CDF/ANAL/EXOTIC/CDFR/9170
March 4, 2008
Version 0.4

Searches for New Physics in the exclusive Dijet plus Missing E_T Event Sample using 2 fb^{-1} and extracted Limits on Scalar Leptoquark Production

Kevin Burkett, Eric James
Fermilab
Pierre-Hugues Beauchemin, Pier-Olivier Deviveiros,
Dan MacQueen, Pierre Savard
University of Toronto

Abstract

We present the results of a signature-based search for new physics using the dijet plus missing transverse energy data sample from 2 fb^{-1} of $p\bar{p}$ collisions at $\sqrt{s} = 1.96$ TeV collected with the Collider Detector at Fermilab. We study the production of events with two high energy jets and large missing energy in a low (high) kinematic regime requiring the scalar sum of the two jet E_T, referred to here as H_T, to be greater than 125 GeV (225 GeV) and event missing E_T above 80 GeV (100 GeV). In both cases, we present comparisons of expected backgrounds with the number of events observed in the data. Based on these results, we extract 95% C.L. lower mass limits on scalar leptoquark production: 189 GeV/c^2 for 1st generation, 185 GeV/c^2 for 2nd generation, and 173 GeV/c^2 for 3rd generation production.

Contents

1 Introduction

Events with large missing transverse energy and one or more energetic jets can be produced in many models of new physics, in addition to Standard Model (SM) production from electroweak and QCD processes. The magnitude of the missing E_T and the number of jets will depend on the specific model of new physics, while the SM backgrounds and instrumental effects can be studied independently. In a previous analysis, we already studied the "monojet" configuration of one energetic jet and large $\not\!\!E_T$ [1]. The present analysis will focus on the exclusive "dijet+$\not\!\!E_T$" signature.

The recent cosmological observation of dark matter [2] is certainly one of the strongest indication of the existance of hitherto undiscovered fundamental degrees of freedom. The fact that the prefered mass scale of these new fields in the popular cold dark matter scenario is the sub-TeV scale [3], significantly increases the importance of searches for excess of events featuring large amount of $\not\!\!E_T$ in the Tevatron and LHC physics programs. In this scenario, the new degrees of freedom that would constitute dark matter candidates must not strongly couple to ordinary matter (SM fields) and must not be short-lived particles. Particles which satisfy these properties are called WIMPs.

In order to guarantee the stability (or metastability) of the WIMPs, the theory describing these new degrees of freedom must contain a discrete symmetry. Such a new discrete symmetry also have the advantage to evade the stringent constaints imposed by LEP on the effect of new particles [4] through the s-channel: the interactions require that new particles get produced in pair. However, exclusive pair production of WIMP candidates is not really interesting from an experimental point of view, since the weakness of their interaction with usual matter fields makes them escape our detector without leaving any signal. A more interesting type of processes, from an experimental point of view, is the production of a pair a new particles which each decay into a WIMP and a known particle. One would therefore search for two visible objects accompagnied by a large amount of $\not\!\!E_T$. In the case of hadron colliders, this kind of event will be more copiously produced when the new particles from which the WIMPs are originating have a non-trival strong interaction charge. In such cases, the particles which will constitute the known part of the decay will also be strongly interacting. Such processes will thus result in at least a pair of jets plus a large amount $\not\!\!E_T$. The exclusive dijet+$\not\!\!E_T$ analysis which is being presented in this note is therefore one of the typical signatures of dark matter production which must be performed.

Now many models with a new discrete symmetry which can provide an explanation for the nature of dark matter predict such a dijet+$\not\!\!E_T$ final state. Supersymmetry is already well-known in the HEP community. In this model, pairs of squarks and gluinos get produced via the strong interaction and each of them further decay into a parton and a neutralino, the WIMP candidate [5]. Universal Extra Dimensions models with conservation of the momentum in the volume of the extra dimensions (K-partity conservation) [6] and Littlest Higgs models with T-parity conservation can also yield completely equivalent dark matter candidates [7] and predict some phenomena with the dijet+$\not\!\!E_T$ signature. All these models are really difficult to disentangle. Since they are not mutually exclusive, they can even all contribute to the final state of interest. Finally, even if dark matter provides ample justification for searching for final states with large $\not\!\!E_T$, other really interesting models predict dijet+$\not\!\!E_T$ final states without providing a viable dark matter candidate. The production of a pair of leptoquarks that each further decay into a quark and a neutrino constitutes one interesting example.

The fact that many different interesting models predict an equivalent dijet+$\not\!\!E_T$ footprint, incites us to pursue a signature-based model-independent search for an excess of dijet+$\not\!\!E_T$ events over Standard Model expectations. In order to do so, exclusive dijet+$\not\!\!E_T$ events selections are chosen without referring to any particular new physics model. They must rather be based on instrumentation criteria and Standard Model background rejection. The key is to maximally reject the backgrounds that are hard to reliably estimate, like the QCD and the non-collision background, in order to avoid unescessary large systematic errors. In order to reduce bias toward a particular model, we also investigate two different kinematic regimes: one low kinematic region (bigger phase space volume) and one higher regime. While the low kinematic region is determined by trigger requirements, the choice of the higher region is somewhat arbitrary. However, the flexibility of model-independent approaches places all kinematic selection choices on the same footing: by construction, any choice will result in a maximal sensitivity to some models, while reducing sensitivity for some others. This is also true within a given theoretical framework. For example, in the squark and gluino mass plane of the MSSM parameter space, there is, by construction, one point for which the low kinematic selections will provide the maximum sensitivity to the model and one point for which the maximum sensitivity will be obtained by our choice of higher kinematic selections, no matter what is this choice. By keeping this model independence we can therefore use the same analysis to provide interpretations to various models. In the following we will interpret the results of our dijet+$\not\!\!E_T$ search in terms of constraints on the mass of scalar leptoquarks and in terms of constraint on the masses of squarks and gluinos in a MSSM, non-mSUGRA, model.

Another particuliarity of the following dijet+$\not\!\!E_T$ analysis is that we will focus on making data-driven estimates of the backgrounds as much as possible. The larger data samples of Run II allow us to use the data for making estimates of the electroweak backgrounds, rather than relying on Monte Carlo predictions. This may increase the statistical error on the background predictions but will protect us from large systematic uncertainties from effects such as the jet energy scale that would arise when using MC-based background predictions. We can however control the statistical uncertainty by a suitable choice of the higher kinematic regime presented above. By using the 2 fb^{-1} of data available to CDF, we will be able to seek a $\sim 5\%$ precision with the low kinematic regime prediction, and choose the high regime such that we get a 10-15% precision on the estimate. Note that the whole measurement procedure that is being used in this analysis, has already been tested in the monojet analysis that we recently performed. Finally note that a CDF RUN II exclusive dijet+$\not\!\!E_T$ analysis has already been performed with 200 pb^{-1} [8], in the context of an optimized Monte Carlo-based search for leptoquarks. Our leptoquark interpretation will allow for some comparison with this earlier analysis.

Since our analysis can be completely decoupled to any new physics interpretation, we will concentrate first, on the study of the Standard Model expectation and instrumental effects, and then we will explain how we can use the results to extract information about leptoquark and supersymmetric models. Our note will therefore be divided as follows: in the next section we will present the dijet+$\not{E}_T$ selections and the data that will be used for this measurement; in section 3 we will discuss the Standard Model contributions to the dijet+$\not{E}_T$ data sample and then present the results of the search. The new physics interpretations will finally be provided in section 4.

2 Data Sample

Based on the dijet+$\not\!\!E_T$ signature that is under study in the present analysis and on the fact that we are interested in the high tail of the $\not\!\!E_T$ distribution, the relevant data for this analysis are those that satisfy high $\not\!\!E_T$ trigger requirement. The data sample on which we will select our dijet+$\not\!\!E_T$ events will thus be collected with the inclusive missing E_T trigger (MET45).

To understand the efficiency of this trigger path for events with reconstructed $\not\!\!E_T$ above a certain treshold X, we studied events collected using unbiased, high E_T lepton triggers and determined the probability for an event to pass the MET45 trigger as a function of the corrected $\not\!\!E_T$. Figure 1 shows the MET45 trigger efficiency bin-per-bin turn-on curve for the run period 0 to 12 (0d, 0h, 0i and 0j, up to run number 241664). For high $\not\!\!E_T$ cut (for example $\not\!\!E_T > 80$ GeV), the events used to get these trigger efficiencies are mostly $W \to \mu\nu + jets$ events for which the missing E_T profile looks really similar to the one of most of the Standard Model background to dijet+$\not\!\!E_T$ events (Z$\to \nu\nu + jets$ and W$\to \ell\nu + jets$). The MET45 trigger efficiency for these SM background contributions can therefore simply be obtain, in a good approximation, from the cumulative efficiency distribution computed from the bin-per-bin trigger efficiency plot. Figure 2 shows this cumulative efficiency distribution for the MET45 trigger. From that, we can see that the MET45 trigger is more than 99% efficient for events with reconstructed $\not\!\!E_T > 80$ GeV. Note however, that this trigger efficiency may vary for specific signal studies. In order to adequately set limit one a specific new physics signal model, we would have to convolute the bin-per-bin efficiency distribution with the missing E_T profile of the signal under study, before computing the

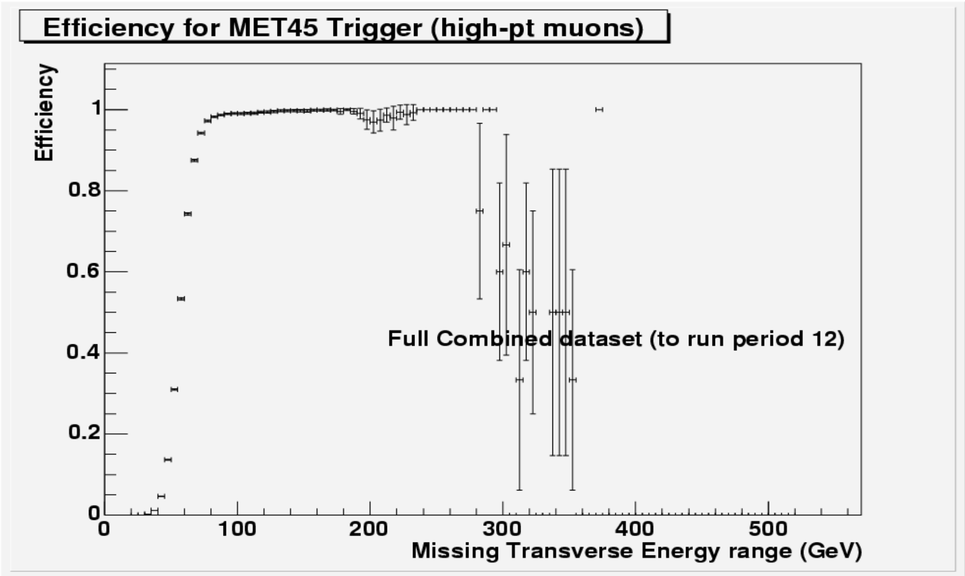

Figure 1: Bin-per-bin efficiency distribution of the MET45 trigger as a function of the reconstructed $\not\!\!E_T$ for data events in the 0d, 0h, 0i and 0j (up to period 12) run ranges (runs 133668 to 241664).

cumulative efficiency. We will discuss this issue in the signal interpretation section.

Note that due to a bug in the L2 trigger table, runs between 178745 and 186598 have been removed. The amount of data associated with this bad run range is ~ 100 pb^{-1}. In this version of the analyses, we use the version 18 good run list for qcd/no silicon. This run list corresponds to integrated luminosities of 2039 pb^{-1} for the MET45 trigger.

The cleanup and event selections used here are similar to those used in the previous monojet measurement [1], since we were already tolerating a low E_T second jet in the monojet analysis. The major difference is the kinematic required for this second jet. The kinematic requirements on the second jet

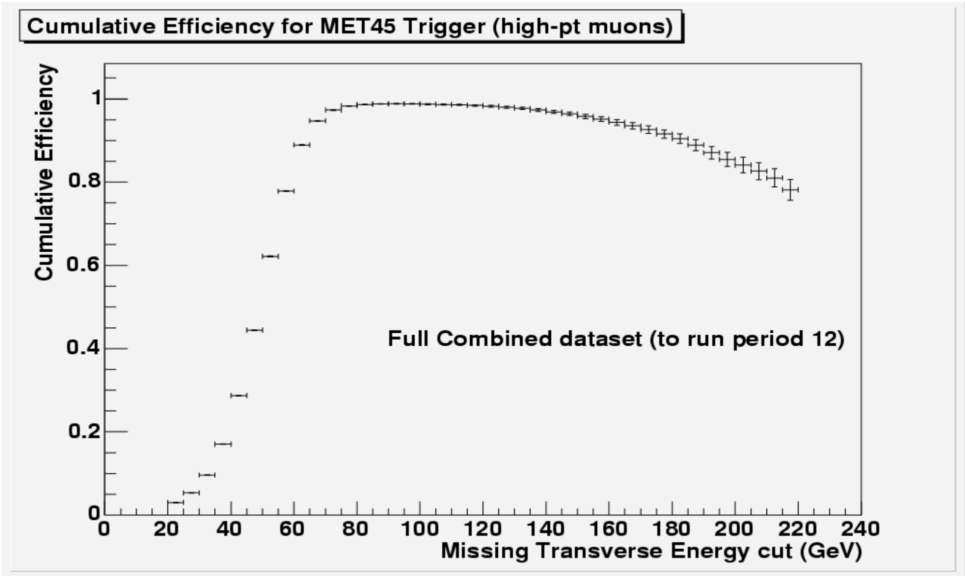

Figure 2: Cumulative efficiency distribution for the MET45 trigger as a function of the reconstructed $\not{E}_T$.

are chosen such that our dijet+$\not{E}_T$ sample stays orthogonal to the monojet sample. Since the jet quality cuts are basically the same in both analyses and that the samples are mutually exclusive, one can see the monojet sample as a controled region for the dijet$\not{E}_T$ analysis.

In the present analysis, jets are reconstructed with the JetClu algorithm using a cone size of 0.7. Only jets with a low-end E_T treshold of 15 GeV, after application of Level 5 Jet Energy Scale correction (JES), are considered in this analysis. The MET45 data contains many events originating from non-collision backgrounds, such beam halo, cosmics, or detector noise. We apply a few simple cuts to clean up the sample and remove the non-collision backgrounds. The set of cuts used for cleanup are the following:

- $|z_{vtx}| < 60$ cm

- > 5 tracks associated with a reconstructed vertex
- Event EM Fraction $\frac{\sum E_T^i \cdot \frac{E_{EM}^i}{E_{TOT}^i}}{\sum E_T^i} > 0.1$

  (sums over all jets with corrected $E_T > 20$ GeV)
- For all jets in the event with corrected $E_T > 15$ GeV:
  - Jet Charge Fraction > 0.1 if $|\eta_{det}| < 1.0$
  - Jet does not point to chimney ($1.05 < \phi < 1.66$ and $0.5 < \eta_{det} < 1.0$) or central crack ($|\eta_{det}| < 0.05$) regions
  - The maximum pseudorapidity of a jet is 2.4 ($|\eta_{det}| < 2.4$)

Jet charge fraction is defined as the sum P_T of all reconstructed tracks located within $\Delta R = 0.7$ of the jet axis divided by the E_T of the jet. For energy deposits in the calorimeter associated with collisions, we expect that in the majority of cases a substantial fraction of the measured E_T will be contained within the measured P_T of the reconstructed, charged tracks pointing in the direction of the observed deposit. The jet charge fraction variable used in the event selection criteria described above is the one included within the standard CDF jet object. Based on studies of our event sample, we determined that this variable as defined in the default CDF software has some problems which make it less than ideal for rejecting the background events in our sample. In particular, the algorithm that calculates this variable does not seem to make any quality cuts on the reconstructed tracks which contribute to the charge fraction sum. In some cases, we observed that a single high p_T track which pointed in the general direction of a jet but far away from the reconstructed event vertex would by itself cause the charge fraction variable for that jet to lie above our cut value. To obtain a cleaner event sample, we wanted to further guarantee that at least some of the reconstructed tracks pointing at a given jet pointed in the direction of the event vertex and satisfied some set of minimal quality requirements. We accomplished this goal by calculating a new jet charge fraction variable (Jet CHF2) for each jet based on tracks found within $\Delta R = 0.7$ of the jet axis that meet the selection criteria listed below.

- Contains 5+ hits on three or more axial COT layers
- Contains 5+ hits on two or more stereo COT layers
- $p_T > 1.0\ GeV/c$
- z_0 is within 10 cm of z-coordinate of event vertex
- $|z_0| < 60\ cm$
- $|d_0| < 0.5\ cm$

For at least one of the jets in our events we require that this jet be central ($|\eta| < 1.0$), that our new jet charge variable (Jet CHF2) > 0.05 for that jet and that at least two tracks (meeting the above criteria) contribute in the calculation of this variable. We also run a cosmic track fitting algorithm [10] that uses COT hit-timing information to check for potential cosmic ray track candidates. Using each reconstructed track with $p_T > 10.0$ GeV/c as a seed track for the algorithm, events are flagged if the algorithm is able to reconstruct an extended track passing through two opposite hemispheres of the detector along a common trajectory [12] based on any of the input seed tracks. Our treatment of the events tagged as cosmics is discussed in Section 4.2.

During data period 8 and 9 (runs 217990 to 230545) problems with the two PMTs of one of the WHA calorimeter tower was responsible for random spikes in that tower. This results in a high energetic fake jet and therefore high fake $\not\!\!E_T$ value for some events (events for which a spike overlap a bunch crossing). To avoid contamination from that instrumental background, we reject any event for which a jet point in the direction of that hot tower ($-1.35 < \eta < -1.15$ and $4.757 < \phi < 4.983$), f or these two specific run periods.

Since we perform an exclusive dijet+$\not\!\!E_T$ analysis, no third jet with corrected E_T above 15 GeV are tolerated in our events (remember that 15 GeV is our low-end jet E_T treshold). In the monojet analysis, we were however tolerating a second jet with E_T below 30 GeV. In order to be orthogonal to that analysis, we impose a low cut of 30 GeV on the second jet E_T. To keep high sensitivity to a maximum of new physics model, we investigate two different kinematic regions. In the low region, we impose a $\not\!\!E_T$ cut of 80 GeV and a H_T cut of 125 GeV, where H_T is defined as the scaler sum of the two jets E_T. These kinematic cuts values are determined by trigger requirements (lowest $\not\!\!E_T$ value for which the MET45 trigger is more than 99% efficient). For the high kinematic region, we require a $\not\!\!E_T$ above 100 GeV, to further remove QCD contribution to the dijet+$\not\!\!E_T$ sample, and a H_T of at least 225 GeV. These selections should allow a 10-15% uncertainty on the full SM background prediction.

In addition, to further reduce QCD background, where the missing E_T is generated by a badly mis-measured jet, we reject events where the $\not\!\!E_T$

direction is close to the second jet, $|\Delta\phi(\text{Jet} - \not{E}_T)| > 0.5$.

Finally, the production of W or Z bosons in association with additional jets can result in events with a topology similar to that of our signal. To reject such events we apply an indirect lepton veto by requiring

- Jet EM Fraction < 0.9 for all jets with $E_T > 20$ GeV
- No reconstructed, isolated tracks with $p_T > 10$ GeV/c

Here an isolated track is based on the calorimeter isolation used for muons. In order for a track to be considered as isolated, it must contain 5+ hits on three or more axial and two or more stereo COT layers and satisfy the following criteria: $p_T > 10$ GeV/c, $|d_0| < 0.5$ cm, and z_0 within 10 cm of the z-coordinate of the event vertex. Tracks passing these requirements are isolated if the measured calorimeter E_T within a $\Delta R = 0.4$ cone around the track (excluding the tower directly in line with the track trajectory) divided by the track p_T is found to be less than 0.1. The cut on jet EM fraction removes events with electrons and the isolated track veto removes both events with muons and additional events with electrons that manage to escape the jet EM fraction cut or land in calorimeter cracks.

2.1 Overview

In the following section we will use these cuts in estimating the Standard Model reactions that have the same final state as our signal. Specifically, W and Z boson QCD associated production and QCD production, using CDF data to normalize the predictions whenever possible.

3 Standard Model Backgrounds

There are a number of Standard Model processes that can contribute events to the dijet plus missing E_T candidate sample. For some processes the origin of the $\not\!\!E_T$ signature is real (coming from neutrinos) and in other cases it is fake (coming from missed or mis-measured particles). The largest background is expected to be from Z+jets, where the Z decays via $Z \rightarrow \nu\nu$. This will produce jets along with real $\not\!\!E_T$. As this background basically mimics our signal, it is irreducible. The next most important background is $W \rightarrow \tau\nu$+jets, which produces events with some real $\not\!\!E_T$ and jets (one jet coming directly from the decay of the τ). W+jets events in which the W decays into an e or μ lead to an additional background in cases where the e or μ is missed by the detector, since this process results in events with jets and a combination of both real and fake $\not\!\!E_T$. We consider these Z and W boson backgrounds along with backgrounds from $t\bar{t}$ and single top production which make a non-negligable contribution to the two jet topology together as the Electroweak backgrounds. Another smaller source of background events in our search channel is QCD jet production. The majority of these events originate from three jet production where one of the jets is badly mis-measured. Similarly, γ + jet production can result in a small number of background events from cases where the γ passes unobserved through a crack in the calorimeter coverage.

Table 1 shows the contributions of the various background processes in the "monojet" search channel (single high E_T jet plus missing E_T) for events containing a jet with E_T greater than 150 GeV. It is clear that the $Z \rightarrow \nu\overline{\nu}$ background is the most significant, followed by the W plus jets backgrounds.

Background	Events
$Z \rightarrow \nu\overline{\nu}$	388 ± 30
$W \rightarrow \tau\nu$	187 ± 14
$W \rightarrow \mu\nu$	117 ± 9
$W \rightarrow e\nu$	58 ± 4
$Z \rightarrow \ell\ell$	8 ± 1
QCD multi-jet	23 ± 20
γ+jet	17 ± 5
Non-collision	10 ± 10
Total expected	808 ± 62
Data observed	809

Table 1: Summary of estimated background contributions and number of observed events for candidate sample used in previous "monojet" search. Candidate selection criteria was single jet with $E_T > 150$ GeV and $\not{E}_T > 120$ GeV.

The expected QCD background is small but not negligible. The excellent agreement between the predicted and observed shapes of the leading jet E_T and event missing E_T distributions in the monojet analysis is shown in Figues 3 and 4. We expect a similar distribution of backgrounds for the dijet plus $\not{E}_T$ topology along with an additional contribution originating from top quark production.

In the sections that follow, we describe the criteria used to select the $W \rightarrow \ell\nu$ and $Z \rightarrow \ell\ell$ ($\ell = e$ or μ) plus jets events used to estimate the major electroweak backgrounds in our signal channel (Monte Carlo is used to estimate the backgrounds from top quark production).

3.1 Electroweak

In $p\bar{p}$ collisions W and Z bosons can be produced in association with hadronic jets [25]. The jets are produced from the high energy partons when they

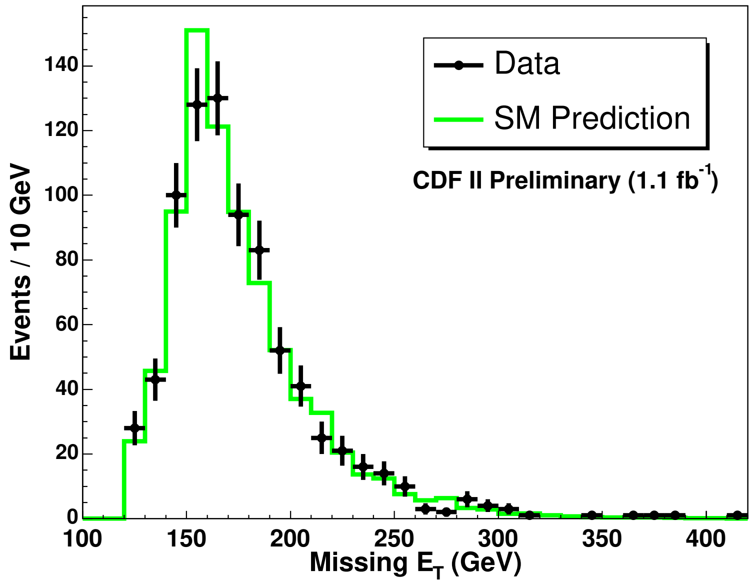

Figure 3: Comparison of the event missing E_T distribution for the 809 events in the E_T >150 GeV and $\not\!\!E_T$ >120 GeV candidate sample used in our optimized searches with the predicted SM distribution.

hadronize after the collisions. As described previously, the major backgrounds to direct graviton production are $Z \to \nu\overline{\nu}$+jets and $W \to \tau\nu$+jets. In the Run I analysis, estimates of the contributions from each background process to the number of observed events in the final candidate sample were made using Monte Carlo. In the current analysis, however, we attempt to as much as possible rely on data-driven estimates of these background contributions to reduce the overall systematic uncertainty on the measurement. Significant uncertainties such as that on our understanding of the relative jet energy scales in data and Monte Carlo can be reduced or eliminated using our data-driven approach which is now possible based on the larger integrated luminosity of the Run II data samples.

Using the high E_T lepton samples, we measure the cross sections for

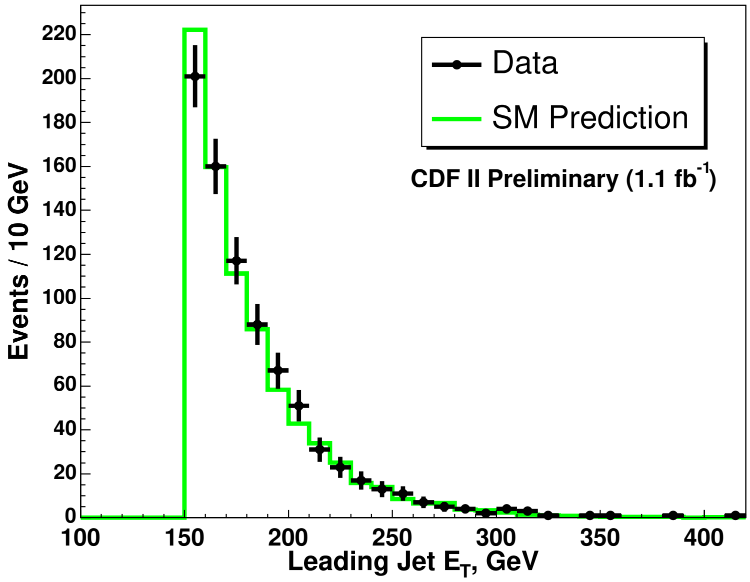

Figure 4: Comparison of the leading jet E_T distribution for the 809 events in the E_T >150 GeV and $\not{E}_T$ >120 GeV candidate sample used in our optimized searches with the predicted SM distribution.

$Z \to ee$+jets and $Z \to \mu\mu$+jets production. We are interested in production cross sections for the subsets of $Z \to ee$ and $Z \to \mu\mu$ events which satisfy the full set of criteria for our final candidate sample as described in Sec. 2 after careful removal and/or modification of all measured event quantities to exclude contributions from the lepton pair produced in the Z boson decay. This criteria forms the definition of the "+jets" requirement attached to our cross section measurements. Using these measured cross sections and the known ratio of the Z boson branching fractions for leptons and neutrinos, we obtain two estimates for the expected number of events in our candidate sample originating from $Z \to \nu\overline{\nu}$+jets production. In addition, using equivalent $W \to e\nu$+jets and $W \to \mu\nu$+jets cross section measurements and a theoretical prediction for R, the ratio of the W+jets and Z+jets production cross sections; we make two additional, independent estimates for the expected number of $Z \to \nu\overline{\nu}$+jets events in our sample. A more precise prediction for the expected background is obtained by combining all four measurements. Estimates for the contribution of the other electroweak backgrounds such as $W \to \tau\nu$+jets are also extracted from the measured W/Z+jets cross sections based on relative acceptance measurements obtained from the Monte Carlo. As previously mentioned, the main advantage of this approach is that it allows us to avoid taking significant systematic uncertainties that would be associated with direct Monte Carlo background estimates including uncertainties in the model for initial- and final-state radiation and the Monte Carlo jet energy scale.

3.1.1 Selection for Z+jets and W+jets Events

For the selection of Z+jets and W+jets events in the data, where the Z or W decays to electrons or muons, we follow closely the event selection of the published electroweak [26] and top analysis, so that blessed scale factors and acceptances can be used.

For selecting $Z \to \mu\mu$+jets and $W \to \mu\nu$+jets events, we first identify muon candidates by selecting tracks that meet the following criteria:

- Contains 5+ hits on three or more axial COT layers
- Contains 5+ hits on two or more stereo COT layers
- $p_T > 20.0$ GeV/c
- $|z_0| < 60$ cm where z_0 is the track impact parameter in z
- $|d_0| < 0.02$ cm (tracks with three or more silicon hits)
  $|d_0| < 0.2$ cm (tracks with two or less silicon hits)

where d_0 is the track impact parameter in $x - y$ with respect to measured beamline position

- E_{EM} = EM energy measured in calorimeter towers intersected by the track [13] < 2 GeV for $P_\mu < 100$ GeV and $< 2+((P_\mu$-100) $\cdot$ 0.0115) GeV for $P_\mu \geq 100$ GeV

- E_{HAD} = HAD energy measured in calorimeter towers intersected by the track [14] < 6 GeV for $P_\mu < 100$ GeV and $< 6+((P_\mu$-100) $\cdot$ 0.0280) GeV for $P_\mu \geq 100$ GeV

- μ_{iso} = Measured calorimeter energy in a $\Delta R = 0.4$ cone around the track after subtracting out the energy in towers directly intersected by the track [15] ≥ 0 GeV

- $\mu_{iso}/p_T < 0.1$

In addition, we run the cosmic ray tagging algorithm [10] described in the previous section on each muon candidate using the associated track as an input seed for the algorithm. We reject muon candidates for which the algorithm is able to reconstruct an extended track passing through two opposite hemispheres of the detector along a common trajectory [12]. For the single muon in $W \to \mu\nu$ plus jets events and one of the two muons in $Z \to \mu\mu$ plus jets events, we make the following additional requirements on the muon candidate:

- Good CMUP muon

  Attached CMU stub with $|\Delta x| < 7$ cm

  Attached CMP stub with $|\Delta x| < 5$ cm

CMU fiducial cuts $dx < 0$ cm,$dz < 0$ cm

CMP fiducial cuts $dx < 0$ cm,$dz <$ -3 cm

No muons with CMP "Bluebeam" stubs

. ($\phi = 60\ ^\circ \rightarrow 70\ ^\circ$) for runs before 154449

- **OR** Good CMX muon

No CMX muons for runs before 150144

No CMX muons in west wedge 14 for runs between 190697 and 209541

CMX fiducial cuts $dx < 0$ cm,$dz <$ -3 cm

Attached CMX stub with $|\Delta x| < 6$ cm

$\rho_{COT} = (((\eta_\mu/|\eta_\mu|) \cdot 155.0) - z_0)/\tan(\pi/2 - \theta_\mu) > 140\ cm$

No muons with CMX "Mini-skirt" ($\phi = 240\ ^\circ \rightarrow 300\ ^\circ$) or

. "Keystone" stubs ($\phi = 75\ ^\circ \rightarrow 105\ ^\circ$)

There is one additional requirement made on the single muon candidate in $W \rightarrow \mu\nu$ plus jets events. We require that the χ^2 per degree of freedom [16] for the muon candidate track fit based solely on COT hit information is less than 2.3 (less than 2.7 for run numbers up to 186598). This additional cut is used to reduce the number of background events in the $W \rightarrow \mu\nu$ plus jets sample in which the muon is produced in the decay of a π or K.

To select $W \rightarrow \mu\nu$+jets events, we require one muon candidate that passes all of the selection criteria listed above. We also require that the event missing $E_T > 20$ GeV. Before making this cut, we apply a number of corrections to the raw missing E_T found in the event record. We first correct the raw missing E_T to account for jet energy corrections applied at the analysis level. Next, the missing E_T is corrected to account for the muon candidate in the event. We add the p_T of the muon candidate and subtract the measured E_T in calorimeter towers traversed by the muon into the event sum E_T calculation. The subtraction of the associated calorimeter energy deposits is done to avoid double-counting. Finally, we require that there is one and only one isolated track (based on the Sec. 2 definition) in each event. This cut is useful for removing $Z \to \mu\mu$ events from the $W \to \mu\nu$ candidate sample.

To select $Z \to \mu\mu$+jets events, we require one muon candidate that passes all of the selection criteria listed above and a second which is only required to pass the initial track selection criteria. The second muon candidate is not required to have an associated stub in any of the muon detectors but must be a high-quality, isolated track with matching, minimum ionizing-like calorimeter deposits. The invariant mass of the muon candidate pair, $M_{\mu\mu}$, is required to be greater than 66 GeV/c^2 and less than 116 GeV/c^2. We also require that the three dimensional opening angle between the two muon candidates $\theta_{3d} = \arccos((P_\mu^1 \cdot P_\mu^2)/(|P_\mu^1||P_\mu^2|)) < 3.07876$ to further reduce any residual cosmic background not already rejected by the cosmic tagging algorithm.

For selecting $Z \to ee$+jets and $W \to e\nu$+jets events, we require electron candidates (tracks matched to energy clusters in the electromagnetic section of the calorimeter) to satisfy the following minimum criteria:

- $E_T^{\mathrm{clus}} > 20$ GeV
- $p_T^{\mathrm{trk}} > 10$ GeV/c

- Track contains 5+ hits on three or more axial COT layers
- Track contains 5+ hits on two or more stereo COT layers
- Track $|z_0| < 60$ cm
- $E_{had}/E_{em} < 0.055 + 0.00045 \cdot E$
- $|\eta_{\rm det}| < 1.0$ [17]
- Not tagged as conversion [18]
- Fiducial CES cut: require FIDELE==1

For the single electron candidate in $W \rightarrow e\nu$+jets events and one of the two electron candidates in $Z \rightarrow ee$+jets events, we make the following additional requirements:

- $E^{\rm clus}/p^{\rm trk} > 0.5$ and $E^{\rm clus}/p^{\rm trk} < 2.0$
- $Q \cdot \Delta x >$ -3.0 cm and $Q \cdot \Delta x < 1.5$ cm [20]
- $|\Delta z| < 3.0$ cm [21]
- Lshr < 0.2 [22]
- $\chi^2_{strip} < 10$ [23]

Finally, for the single electron candidate in $W \rightarrow e\nu$+jets events we additionally require

- $E_T^{\rm clus} > 25$ GeV
- $e_{iso}/E_T^{\rm clus} < 0.1$ [19]

To select $W \to e\nu$+jets events, we require one electron candidate passing all of the selection criteria listed above and total event missing $E_T > 25$ GeV. As in the case of muon events, the raw missing E_T is first corrected to account for jet energy corrections applied at the analysis level. In the case of electron events, however, the applied jet corrections are not appropriate for the one reconstructed jet associated with the electron candidate (electron cluster energies are properly calibrated in offline event reconstruction); and therefore the modification of the event missing E_T is done using an uncorrected energy for the jet that corresponds to the electron candidate. Also, as in the case of muon events, we require that there is no more than one isolated track (based on the Sec. 2 definition) in each event.

For selecting $Z \to ee$+jets events, we require at least one electron candidate that passes all selection criteria and a second that at a minimum satisfies the first set of criteria listed above. In addition, the invariant mass of the electron candidate pair, M_{ee}, is required to be greater than 66 GeV/c^2 and less than 116 GeV/c^2. We refer to the resulting set of candidate events as our "tight-loose" $Z \to ee$+jets (default) sample. For making comparisons, we also utilize a "tight-tight" $Z \to ee$+jets sample in which both electron candidates are required to pass the full set of selection criteria given above

3.1.2 Measurement of Z+jets and W+jets Cross Sections

We measure inclusive cross sections using the W and Z candidate samples described in the previous section and compare the results against published Run II measurements to validate our event selection and techniques for measuring selection efficiencies and contributions from background processes in the samples. Then, we apply the complete set of cuts used to construct each of the missing E_T plus jet(s) candidate samples described previously in Sec. 2 to the events in our $W \to \ell\nu$+jets and $Z \to \ell\ell$+jets samples after careful removal and/or modification of all measured event quantities to exclude contributions from the reconstructed leptons in these events. For example, events in these samples are required to have no *extra* isolated tracks, beyond those directly associated with the lepton candidates, as opposed to no isolated tracks whatsoever. In the electron samples, jets matched to reconstructed electron candidates are removed from the list of jets used in event selection. Similarly, the applied missing E_T selection criteria are based on modified values in which energies associated with the reconstructed leptons in the events are removed. The final cross section measurements used to extract the electroweak background fractions for our final candidate samples are those based on the samples selected using the full set of kinematic selection criteria. We note that the candidate samples used to make these measurements are obtained using Version 18 good run lists. Using these good run lists, the integrated luminosity of the electron dataset is 2148 pb^{-1} (375 pb^{-1} for Period 0, 724 pb^{-1} for Periods 1-7, and 1047 pb^{-1} for Periods 8-12) and the integrated luminosity of the muon dataset is 2019 pb^{-1} (373 pb^{-1} for Period 0, 675 pb^{-1} for Periods 1-7, and 967 pb^{-1} for Periods 8-12).

We measure the acceptance of our W/Z+jet candidate events using simulated Alpgen samples. The utilized samples are $Z \to \ell\ell$ and $W \to \ell\nu$ plus i-parton(s) where $\ell = e$ or μ and $i = 1$ to 4. "Double-counted" events are removed from the sample using the standard procedure developed by the top group. These events come about due to the fact that the CDF simulation adds final state radiation subsequent to event generation. For example, a two parton event with an additional final state radiation can in some cases be the equivalent of a generator-level event in the three parton sample. These duplicate events are removed from the samples via the top group perscription. Subsequent to this event removal, it is also necessary to normalize the different samples with respect to one another. The procedure is to assign each event a weight taken from the theoretical cross section of the corresponding sample divided by the total number of remaining events in the sample. The overall normalization of the sample is not important, but this procedure ensures that the relative contributions of the various i-parton samples is correct. Note that the run periods modeled by the Alpgen Monte Carlo samples are 0 to 8, while the data used in this analysis encompasses periods 0 to 12. Since the luminosity profile of the later run periods is higher than that of the earlier run periods, it's important to check if there is a significant luminosity dependence on the acceptances that we measure. In particular, because of the higher number of mean interactions per collision during these later run periods, one might expect an effect on the efficiency for certain lepton selection criteria (isolation being one example). To check the magnitude of this effect, we re-weight the events in the existing MC as a function of the number of observed vertices in the event to reproduce the distribution observed over all data periods (0 to 12). The re-weighting procedure yields acceptances that agree within statistical uncertainties ($\sim 1\,\%$) with the values obtained from the non-weighted events. There is one additional technical detail regarding the Z boson Alpgen samples. These samples are generated with a mass window of 75 to 105 GeV/c^2 which is smaller than that used to select Z+jets candidate events from the data (66 to 116 GeV/c^2). Since a mass requirement is made in both the numerator and denominator of the acceptance calculation, the effect of not having the extended mass range in the MC sample is expected to be a second order effect. To check this assumption, we use Pythia samples generated over a much wider mass range and determine the acceptances obtained from the subsets of events within the two mass ranges. We use the observed difference to obtain a small scale factor (1.001) which gets applied to the acceptances measured from the Alpgen samples.

The definition of the denominator used in our acceptance calculations is the number of W/Z+jets events (post-simulation and reconstruction) that satisfy the full set of dijet plus missing E_T selection criteria after the removal of all detector quantities associated with the leptons produced in the boson decay. The numerator is defined as the subset of these events that additionally satisfy the lepton requirements used in the selection of our W/Z+jets candidate events. Based on these definitions, we obtain a lepton-only acceptance for the subset of W/Z+jets events that otherwise satisfy our dijet plus missing E_T criteria. Background contributions are obtained from the corrsponding MC samples (Alpgen for W/Z+jets and Pythia for both $t\bar{t}$ and single top production) except in the case of backgrounds originating from QCD multi-jets. The QCD background in the $W \rightarrow \mu\nu$+jets candidate sample is extracted from the standard extrapolation technique based on the distribution of data events in $\not\!\!E_T$ versus lepton isolation. For the equivalent electron decay channel where this background is much more significant, we estimate the QCD background using a new technique based on fitting the lepton isolation distribution for signal and background contributions. The new background method is described in more detail in CDF8722 [27]. The contribution of QCD background events to the $Z \rightarrow \ell\ell$+jets samples is estimated using the number of observed like-sign events (using the Monte Carlo to correct for the number of expected like-sign events from Z decays). This background is found to be negligible in the case of our $Z \rightarrow \mu\mu$+jets candidate sample. Efficiency scale factors are applied to each cross section measurement to account for event trigger efficiencies and observed differences in lepton selection cut efficiencies for data and Monte Carlo. Because we utilize standard CDF lepton selection requirements, we apply the standard blessed scale factors originating from the joint physics group. For the later run periods, we use the standard perscription to correct measured trigger efficiencies to account for the effects of luminosity enabling and dynamic prescaling on the high p_T muon triggers run during these periods. The applied scale factors are independent of any jet selection requirements but do change slightly as a function of the leading jet E_T cut for the muon cross section measurements. These small differences are due to the fact that we measure independent scale factors for CMUP and CMX muons and the relative fractions of CMUP and CMX events do vary as a function of the leading jet E_T. Also note that the scale factors used for the inclusive measurements differ from those used in the other cross section measurements. One reason is that the inclusive Monte Carlo samples for the 0d run period were produced with version 5 of the offline software (the samples used for the non-inclusive measurements were generated with version 6 over the entire run range). In addition, the scale factors for the inclusive measurements include an efficiency correction (data versus Monte Carlo) for the selection of a reconstructed vertex within 60 cm of the interaction point. In the other measurements, this particular requirement is part of the dijet plus missing E_T selection criteria which define the denominator of the acceptance calculation. The input parameters and results of the inclusive cross section measurements made to verify our event selection and efficiency scale factors taken from the joint physics group are shown in Table 2 for three different run periods encompassing the full dataset used in this analysis. The same information for our W/Z plus jets cross section measurements where the jet and $\not\!\!E_T$ requirements are the same as those used to select our dijet plus missing E_T event samples is shown in Table 3.

The quoted uncertainties on the cross section measurements are mostly statistical but do include systematics originating from the background estimates. The inclusive W/Z cross section can be compared between channels and run periods. In general, we find good agreement between the different measurements and with previously measured values. For the W/Z+jets cross section measurements, we expect to observe agreement between the different channels, but not necessarily between different time periods. This expected discrepancy is due to the fact that the cross section which we measure is partially defined by objects that are reconstructed in the detector. In particular, we measure the cross sections for events with a reconstructed jet above some E_T threshold. The cross section defined in this way will have at least some luminosity dependence since the presence of extra minimum bias interactions will contribute additional underlying energy within each jet cone, essentially lowering the nominal jet E_T threshold. Since we are using these cross section measurements to predict other backgrounds within the same data sample, these are in fact the correct measurements to use. However, when combining measured cross sections from different run periods, we therefore use luminoisty-weighted rather than direct averages.

The final values of $\sigma(W)$ and $\sigma(Z)$ used in the background estimates are those based on the full set of dijet plus missing E_T selection criteria. However, correction factors must be applied to the measured cross sections prior to

$W \to e\nu$	P0 (0d data)	P1-P7 (0h+0i data)	P8-P12 (0i+0j data)
Acceptance	0.1775 ± 0.0001	0.1775 ± 0.0001	0.1752 ± 0.0001
Raw Data	190910	363819	498892
Background	$4.49 \pm 0.97\%$	$4.78 \pm 1.11\%$	$5.86 \pm 1.53\%$
Efficiency SF	0.9406 ± 0.0086	0.9725 ± 0.0084	0.9397 ± 0.0113
Luminosity	375 pb^{-1}	724 pb^{-1}	1047 pb^{-1}
$\sigma(W)$[pb]	2912 ± 40	2772 ± 41	2724 ± 55
$W \to \mu\nu$	P0 (0d data)	P1-P7 (0h+0i data)	P8-P12 (0i+0j data)
Acceptance	0.1832 ± 0.0002	0.1808 ± 0.0002	0.1823 ± 0.0001
Raw Data	183745	340118	494975
Background	$12.52 \pm 0.70\%$	$12.53 \pm 0.74\%$	$13.05 \pm 0.92\%$
Efficiency SF	0.8565 ± 0.0058	0.8852 ± 0.0042	0.8659 ± 0.0131
Luminosity	373 pb^{-1}	675 pb^{-1}	967 pb^{-1}
$\sigma(W)$[pb]	2746 ± 30	2754 ± 28	2819 ± 52
$Z \to ee$	P0 (0d data)	P1-P7 (0h+0i data)	P8-P12 (0i+0j data)
Acceptance	0.0876 ± 0.0002	0.0876 ± 0.0002	0.0882 ± 0.0001
Raw Data	8819	16853	23760
Background	$0.6 \pm 0.1\%$	$0.7 \pm 0.1\%$	$2.3 \pm 0.1\%$
Efficiency SF	0.9919 ± 0.0092	1.0237 ± 0.0098	1.0106 ± 0.0076
Luminosity	375 pb^{-1}	724 pb^{-1}	1047 pb^{-1}
$\sigma(Z)$[pb]	269 ± 4	258 ± 3	249 ± 3
$Z \to \mu\mu$	P0 (0d data)	P1-P7 (0h+0i data)	P8-P12 (0i+0j data)
Acceptance	0.1436 ± 0.0003	0.1431 ± 0.0002	0.1442 ± 0.0002
Raw Data	12748	23503	34378
Background	negl.	negl.	$0.15 \pm 0.03\%$
Efficiency SF	0.9088 ± 0.0074	0.9385 ± 0.0073	0.9418 ± 0.0166
Luminosity	373 pb^{-1}	675 pb^{-1}	967 pb^{-1}
$\sigma(Z)$[pb]	262 ± 3	259 ± 3	261 ± 5

Table 2: Input parameters and results for the W/Z inclusive cross section measurements made to verify our event selection and efficiency scale factors obtained from the joint physics group. The measurements are made for three separate run periods encompassing the full data sample.

$W \to e\nu$	$H_T > 125, \not{E}_T > 80$	$H_T > 225, \not{E}_T > 100$
Acceptance	0.2465 ± 0.0035	0.3093 ± 0.0122
Raw Data	508	65
Background	$30.0 \pm 5.8\%$	$28.9 \pm 4.7\%$
Efficiency SF	0.9606 ± 0.0096	0.9606 ± 0.0096
$\sigma(W)$[pb]	0.700 ± 0.074	0.072 ± 0.014
Cor. Factor	0.972 ± 0.017	1.005 ± 0.043
Cor. X-Sec	0.680 ± 0.073	0.073 ± 0.014
$W \to \mu\nu$	$H_T > 125, \not{E}_T > 80$	$H_T > 225, \not{E}_T > 100$
Acceptance	0.2591 ± 0.0040	0.3228 ± 0.0132
Raw Data	363	40
Background	$25.5 \pm 1.7\%$	$33.0 \pm 4.3\%$
Efficiency SF	0.8674 ± 0.0128	0.8798 ± 0.0146
$\sigma(W)$[pb]	0.596 ± 0.046	0.047 ± 0.012
Cor. Factor	1.071 ± 0.016	0.993 ± 0.042
Cor. X-Sec	0.638 ± 0.050	0.047 ± 0.012
$Z \to ee$	$H_T > 125, \not{E}_T > 80$	$H_T > 225, \not{E}_T > 100$
Acceptance	0.1546 ± 0.0049	0.2028 ± 0.0080
Raw Data	23	4
Background	$24.3 \pm 8.5\%$	$29.8 \pm 24.3\%$
Efficiency SF	1.0176 ± 0.0071	1.0176 ± 0.0071
$\sigma(Z)$[pb]	0.052 ± 0.016	0.006 ± 0.005
Cor. Factor	0.962 ± 0.022	0.933 ± 0.038
Cor. X-Sec	0.050 ± 0.015	0.006 ± 0.005
$Z \to \mu\mu$	$H_T > 125, \not{E}_T > 80$	$H_T > 225, \not{E}_T > 100$
Acceptance	0.2517 ± 0.0078	0.3322 ± 0.0122
Raw Data	42	7
Background	$4.9 \pm 1.0\%$	$2.6 \pm 0.6\%$
Efficiency SF	0.9470 ± 0.0343	0.9179 ± 0.0632
$\sigma(Z)$[pb]	0.083 ± 0.014	0.011 ± 0.004
Cor. Factor	1.117 ± 0.015	1.114 ± 0.041
Cor. X-Sec	0.093 ± 0.016	0.012 ± 0.005

Table 3: Input parameters and results for the W/Z plus jets cross section measurements where the jet and $\not{E}_T$ requirements are the same as those used to select our dijet plus missing E_T event sample. The integrated luminosities of the electron and muon samples are 2148 pb^{-1} and 2017 pb^{-1}, respectively.

extracting our final estimates for the $Z \to \nu\nu$ +jets background in this event sample. The correction factors, obtained from the simulated event samples, are used to account for small differences between the $Z \to \nu\nu$ and $Z \to \ell\ell$ event topologies. For example, when we exclude jets associated with electrons in $W \to e\nu$+jets and $Z \to ee$+jets events, we are excluding some fraction of the available phase space for extra jets within the event (phase space that is available within $Z \to \nu\nu$ events). Similarly, electroweak radiation from leptons can produce extra jets within an event that would not be seen in association with neutrinos. In the case of our measured $Z \to \ell\ell$ cross sections, we directly compare the fractions of $Z \to \nu\nu$ and $Z \to \ell\ell$ Monte Carlo events satisfying the full set of monojet selection crtieria (subsequent to the removal of leptons in the case of $Z \to \ell\ell$ events). The correction factors applied to the measured cross sections are simply the ratio of these measured event fractions. In order to calculate correction factors for the $W \to \ell\nu$ cross section measurements, we assume that the effects which necessitate the corrections scale linearly with respect to the number of charged leptons in the final state (correction factors for $W \to \ell\nu$ cross sections are roughly a factor of two lower than those for $Z \to \ell\ell$ cross sections). The final correction factors are small (on the order of 5-10 %). The correction factor uncertainties include a statistical component based on the size of the Monte Carlo samples used to measure these factors and a systematic component obtained from observed differences in the correction factors measured from independent samples generated using the Alpgen and Pythia generators.

The combined, corrected W/Z+jet cross sections using the full dijet plus missing E_T selection criteria are summarized in Table 4 for the measurements made in both the electron and muon decay channels. We observe good agree-

Cross Section (pb)	$H_T > 125, \not\!\!E_T > 80$	$H_T > 225, \not\!\!E_T > 100$
$\sigma(W \to e\nu + \text{jets})$	0.68 $\pm$ 0.07	0.073 $\pm$ 0.014
$\sigma(W \to \mu\nu + \text{jets})$	0.64 $\pm$ 0.05	0.047 $\pm$ 0.012
$\sigma(W \to \ell\nu + \text{jets})$	0.65 $\pm$ 0.04	0.057 $\pm$ 0.009
$\sigma(Z \to ee + \text{jets})$	0.05 $\pm$ 0.02	0.006 $\pm$ 0.005
$\sigma(Z \to \mu\mu + \text{jets})$	0.09 $\pm$ 0.02	0.012 $\pm$ 0.005
$\sigma(Z \to \ell\ell + \text{jets})$	0.07 $\pm$ 0.01	0.009 $\pm$ 0.003

Table 4: Combined W/Z+jet cross section measurements used to estimate backgrounds in the dijet plus missing E_T.

ment between the two channels, and therefore combine the electron and muon measurements, the uncertainties of which are uncorrelated. These final combined values which are then used to extract the final background estimates for our candidate sample are also given in Table 4.

3.1.3 Estimate of $Z \to \nu\overline{\nu}$+jets background

In principle, the cross-section for $Z \to \nu\overline{\nu}$+jets is given simply by

$$\sigma(Z \to \nu\overline{\nu} + \text{jets}) \;=\; 6 \times \sigma(Z \to \ell\ell + \text{jets})$$

or

$$\sigma(Z \to \nu\overline{\nu} + \text{jets}) \;=\; 6 \times \sigma(W \to \ell\nu + \text{jets}) \times \mathrm{R}$$

so the measured cross-sections for W and Z+jets can be used to obtain the cross-section for $Z \to \nu\overline{\nu}$+jets. To use $\sigma(W)$ and profit from the larger statistics in those samples, we need reliable values for R. This is a robust quantity to calculate since many theoretical uncertainties cancel or are significantly reduced in the ratio. After discussions with experts [28] we decided to use MCFM [29] for our calculations of R.

In order to determine the values of R appropriate for the kinematic criteria used in the selection of our dijet plus missing E_T candidate sample, we use

Candidate Sample	$H_T > 125, \not\!\!E_T > 80$	$H_T > 225, \not\!\!E_T > 100$
Calculated R	10.17	10.14
Monte Carlo Statistics	$\pm$ 0.05	$\pm$ 0.19
Uncertainty from PDFs	$\pm$ 0.05	$\pm$ 0.05
Uncertainty from Renormalization Scale	$\pm$ 0.17	$\pm$ 1.05
Uncertainty from Energy Scale	$\pm$ 0.16	$\pm$ 0.16
Total Uncertainty	$\pm$ 0.26	$\pm$ 1.08

Table 5: Values for R obtained from MCFM theoretical calculation.

MCFM to generate W and Z plus 2 parton cross sections at next-to-leading order (NLO). We use this generation to produce cross section-weighted H_T distributions corresponding to both the W and Z production processes. We then integrate the cross section above the H_T cut used to define the candidate samples for each of the processes and divide the W boson result by the Z boson result to obtain a theoretical value of R corresponding to each candidate sample. In order to determine systematic uncertainties, we redo the calculations using different PDF models and different choices for the renormalization scales. Since the generator-level H_T scale is not necessarily matched exactly to the reconstructed H_T scale in data, we also assign a jet energy scale uncertainty to account for potential differences. This number is obtained by looking at the variation in R over a range of H_T values consistent with the jet energy scale uncertainties in data and Monte Carlo. Table 5 shows the R values coming from our theoretical calculation along with the associated uncertainties due to PDFs, renormalization scale, and energy scale. Using this approach, we combine our statistically independent W+jets and Z+jets cross section measurements and obtain the best possible estimates for the number of $Z \rightarrow \nu\overline{\nu}$+jets background events in the 2 fb^{-1}

$Z \to \nu\nu$ Prediction	$H_T > 125, \not\!\!E_T > 80$	$H_T > 225, \not\!\!E_T > 100$
Sample Luminosity	2039 pb^{-1}	2039 pb^{-1}
From $\sigma(Z \to \ell\ell + \text{jets})$	836 ± 129	111 ± 41
From $\sigma(W \to \ell\nu + \text{jets})$	767 ± 52	68 ± 13
Combined Estimate	777 ± 49	72 ± 12

Table 6: Predicted numbers of $Z \to \nu\nu$ events.

dijet plus missing E_T candidate sample.

Table 6 shows the expected number of $Z \to \nu\nu$+jets events in each of our final candidate samples based solely on the measured $Z \to \ell\ell$+jets and $W \to \ell\nu$+jets cross sections and a combined result based on both.

3.1.4 Estimate of remaining W/Z+jets Backgrounds

Starting from our measurements of the $Z \to \ell\ell$+jets and $W \to \ell\nu$+jets cross sections, we can also estimate the contributions of the other W/Z+jets backgrounds to the dijet plus missing E_T candidate sample. For example, the background from $W \to \mu\nu$+jets can be estimated using the measured $W \to \mu\nu$+jets cross section and the fraction of events (as determined from Monte Carlo) in which the muon track is not reconstructed or otherwise fails to satisfy the lepton veto requirements. To obtain our prediction, we multiply the measured $W \to \mu\nu$+jets cross section (before corrections) by the fraction of events in which the muon is "lost", the integrated luminosity of the candidate sample, and a trigger efficiency correction to account for the small measured inefficiency in the MET45 trigger for events with reconstructed $\not\!\!E_T$ above the threshold used in the selection of the candidate samples. In the case of the lower kinematic region, for reference, the fraction of events with a lost muon is estimated to be 0.33 ± 0.01. A similar procedure is used to estimate the $W \to e\nu$+jets background. Due to the wider coverage of the calorimeter, electrons are less likely to be lost ($20.8 \pm 0.3\%$ of events in the lower kinematic range) and therefore their overall contribution to the dijet plus missing E_T sample is less. The background from $W \to \tau\nu$+jets is a bit more complicated because there are contributions both from cases where the τ is lost and where the τ is identified as a jet. In this case we compare the number of $W \to \tau\nu$+jets events in MC that pass our dijet plus missing E_T selection cuts with respect to the number of $W \to \mu\nu$+jets events that pass the same selections. This procedure provides us with an estimate for the "loss" of $W \to \tau\nu$+jets events with respect to the measured $W \to \mu\nu$+jets cross section ($54.6 \pm 0.8\%$ in the lower kinematic region). The $Z \to \ell\ell$+jets background coming from events with two lost leptons is significantly smaller but estimated in the identical manner based on the measured $Z \to \ell\ell$+jets cross sections.

3.1.5 Top Quark Background

The background contributions from the $t\bar{t}$ and single top quark production processes are the one electroweak component estimated directly from MC. We use Pythia to model the production processes including both s and t-channel single top components. In the case of $t\bar{t}$ production, we normalize the total cross section to match the CDF measurement based on 700 pb^{-1} of Run II data. For the single top samples, we normalize to the values obtained from NLO theoretical calculations. Systematic uncertainties assigned to the estimated top quark backgrounds include cross section uncertainties, luminosity uncertainties, jet energy scale uncertainties, and uncertainties on the top quark mass.

Candidate Sample	$H_T > 125, \not\!\!E_T > 80$	$H_T > 225, \not\!\!E_T > 100$
Sample Luminosity	2039 pb^{-1}	2039 pb^{-1}
$Z \to \nu\overline{\nu}$ Events	777 ± 49	71 ± 12
$W \to \tau\nu$ Events	669 ± 42	50 ± 8
$W \to \mu\nu$ Events	399 ± 25	33 ± 5
$W \to e\nu$ Events	256 ± 16	14 ± 2
$Z \to \ell\ell$ Events	29 ± 4	2 ± 0
Top Quark Production	74 ± 9	11 ± 2
Total Events	2206 ± 136	183 ± 27

Table 7: Summary of estimated electroweak background contributions to the dijet plus missing E_T candidate samples.

3.1.6 Summary of Electroweak Background Estimates

The estimated electroweak background contributions to each of the candidate samples used in our searches are summarized in Table 7.

3.1.7 Cross checks of Alpgen W/Z+parton Monte Carlo

The data-driven technique that we use to measure the electroweak background is chosen to minimize dependence on the Monte Carlo. As discussed previously, however, we do rely on Monte Carlo to determine the acceptance of the lepton selection requirements used to select the W/Z+jets candidate samples utilized for our background estimates. Therefore, it is important to cross check the Alpgen modeling of the leptons in these samples. Comparisons of the electron kinematic distributions between data and Monte Carlo in the $W \to e\nu$+jets and $Z \to ee$+jets candidate samples are shown in Figs. 5 and 6. The equivalent comparisons for muons in the $W \to \mu\nu$+jets and $Z \to \mu\mu$+jets candidate samples are shown in Figs. 7 and 8. The observed agreement is excellent in both cases. Because of our measurement technique, the quality of the Monte Carlo model for the jet and missing E_T distributions in these samples is less important. However, as illustrated in Figs 9 - 11, we do observe good agreement between data and Monte Carlo in the jet kinematic distributions obtained from the $W \rightarrow \mu\nu$+jets and $Z \rightarrow \mu\mu$+jets candidate samples. Note that here we restrict ourselves to looking at these distributions in the muon samples since we do not have a good way to model the kinematic shapes of the QCD background contribution to the electron samples which is significant. Comparisons of the $Z \rightarrow \mu\mu$+jets candidate sample invariant mass distribution and the $W \rightarrow \mu\nu$+jets cnadidate sample transverse mass distributions also showing excellent agreement between data and Monte Carlo are shown in Fig. 12.

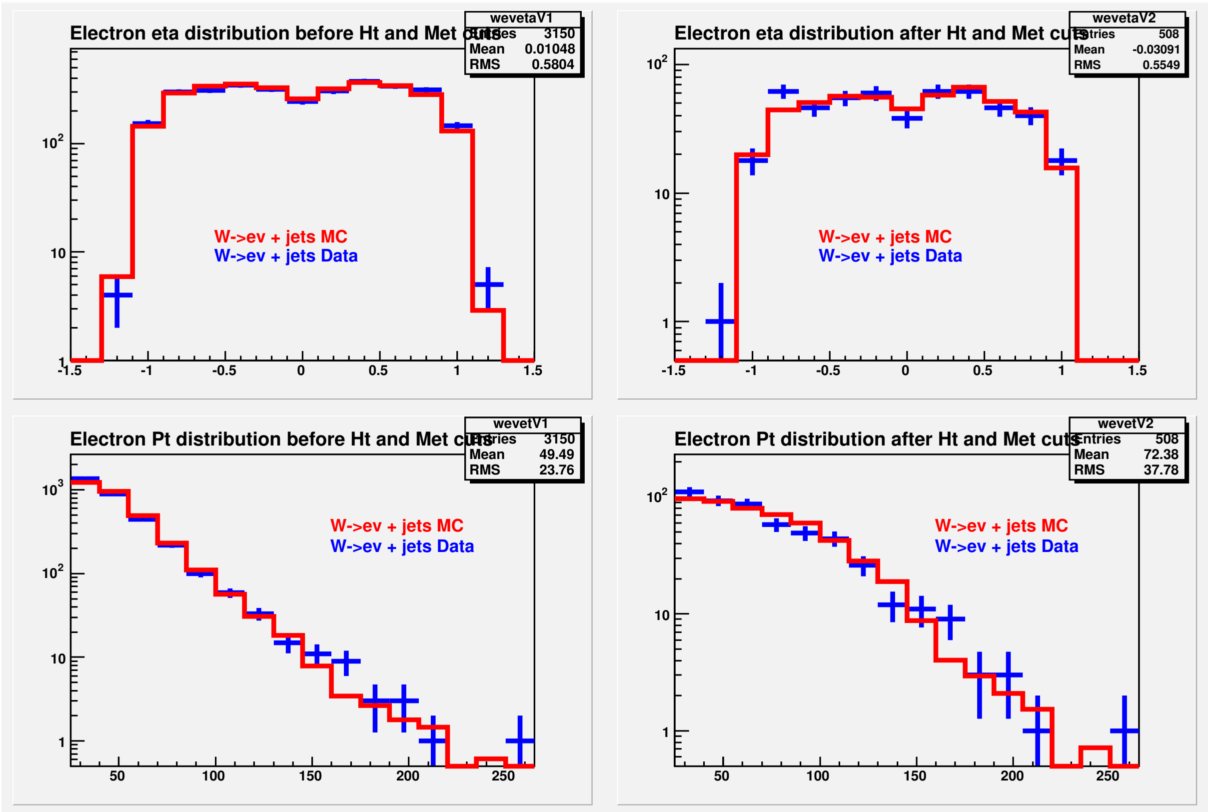

Figure 5: Comparison of electron kinematic distributions between Alpgen Monte Carlo and data for $W \to e\nu$+jets candidate sample.

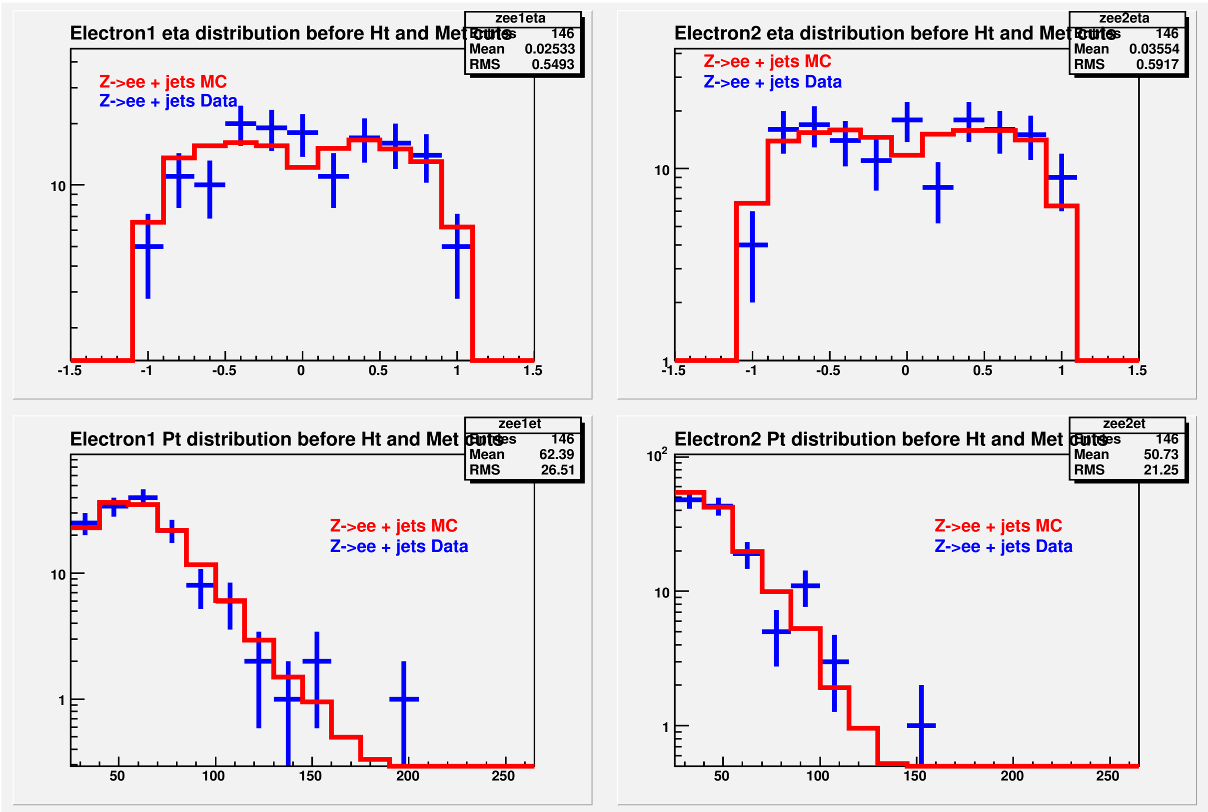

Figure 6: Comparison of electron kinematic distributions between Alpgen Monte Carlo and data for $Z \to ee$+jets candidate sample.

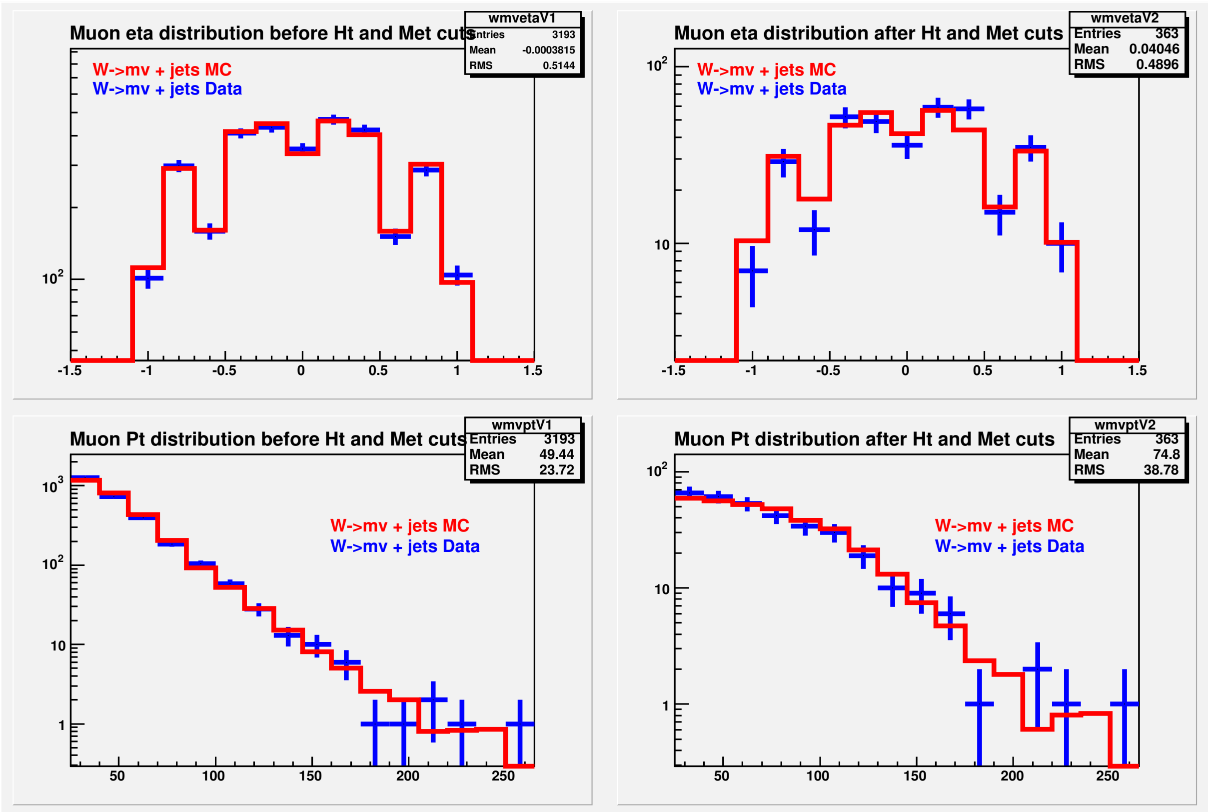

Figure 7: Comparison of muon kinematic distributions between Alpgen Monte Carlo and data for $W \to \mu\nu$+jets candidate sample.

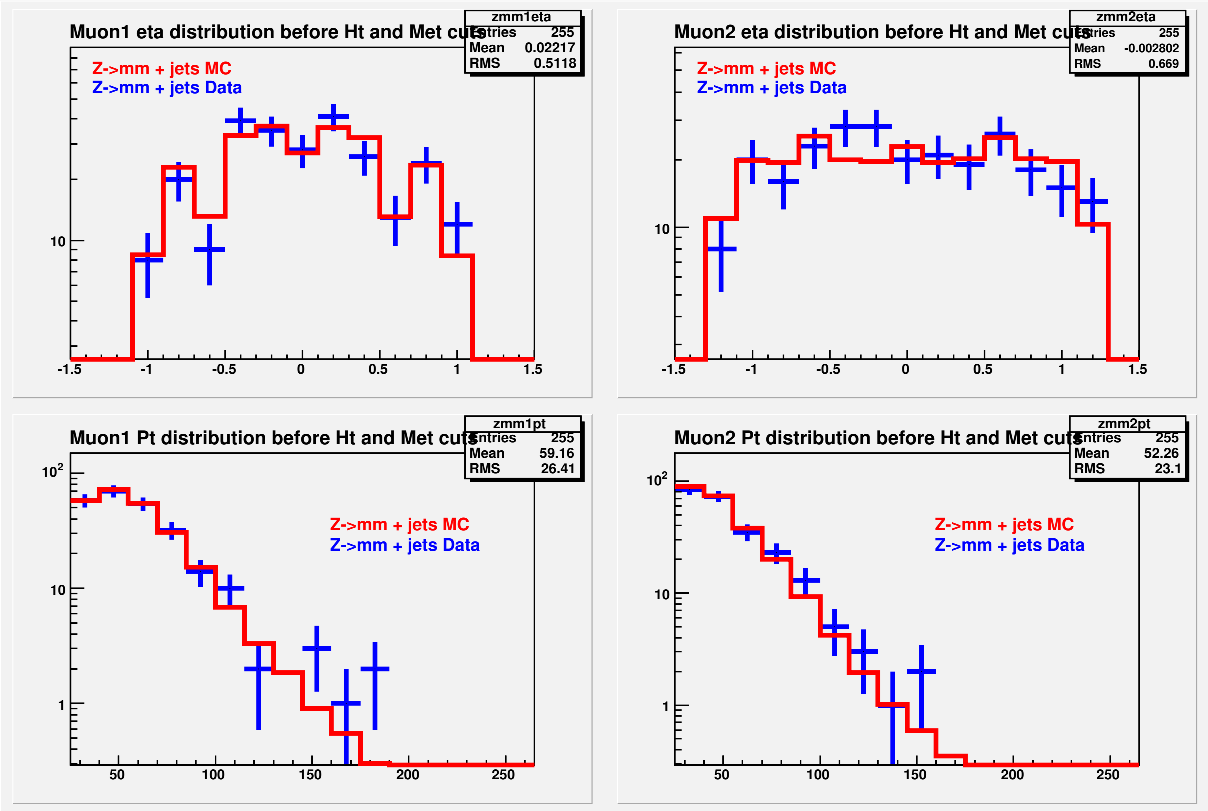

Figure 8: Comparison of muon kinematic distributions between Alpgen Monte Carlo and data for $Z \to \mu\mu$+jets candidate sample.

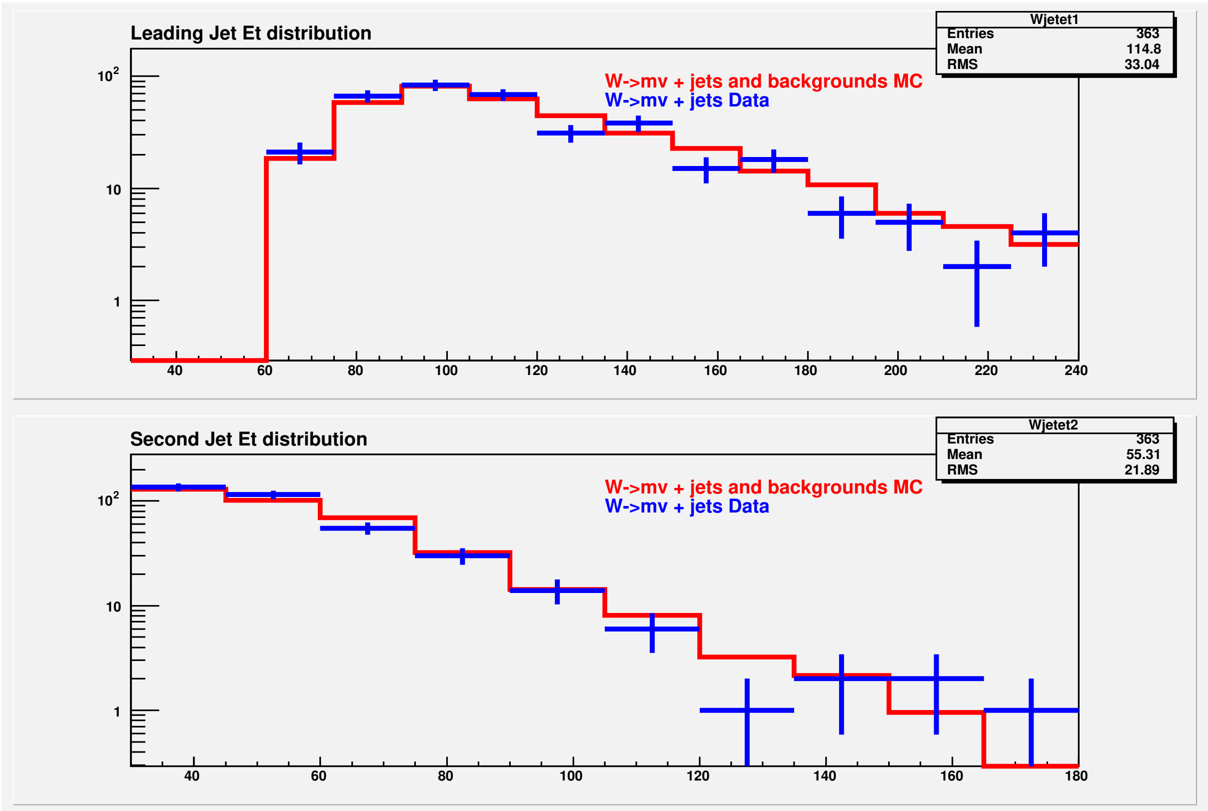

Figure 9: Comparison of jet kinematic distributions between Alpgen Monte Carlo and data for $W \to \mu\nu$+jets candidate sample.

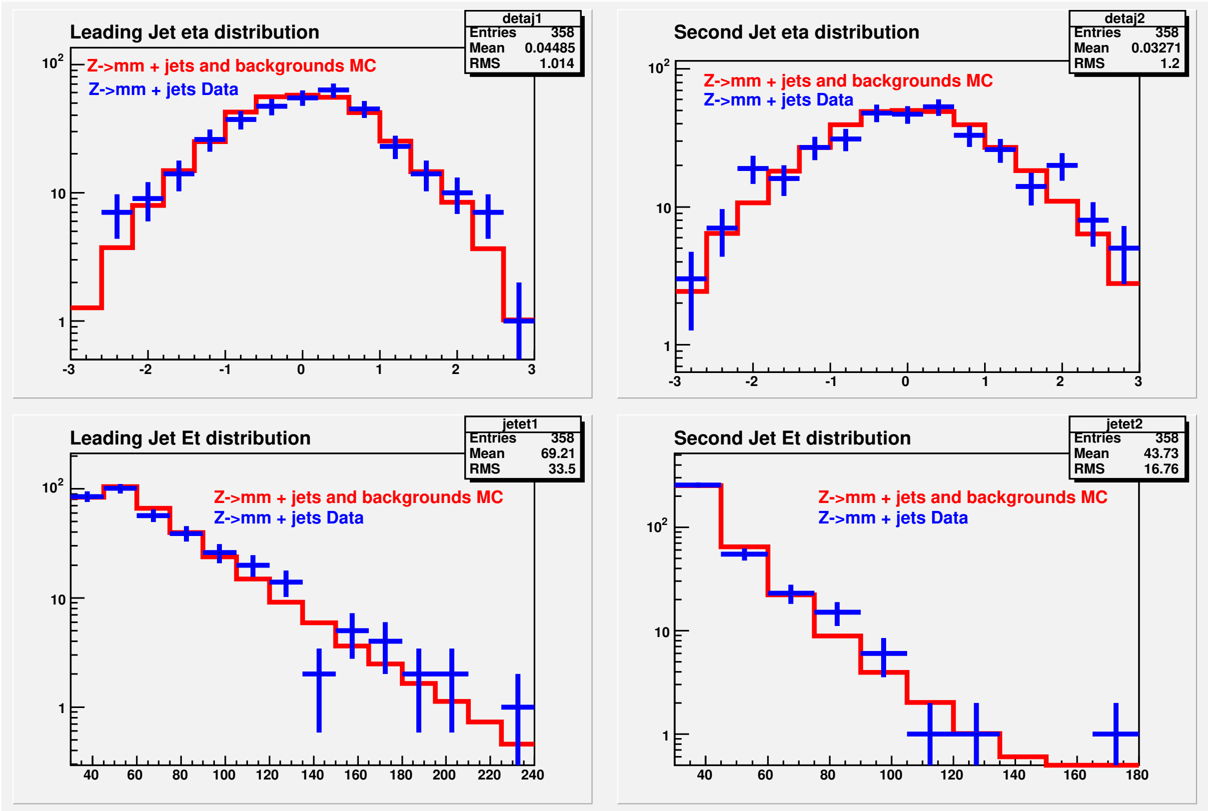

Figure 10: Comparison of jet kinematic distributions (I) between Alpgen Monte Carlo and data for $Z \to \mu\mu$+jets candidate sample.

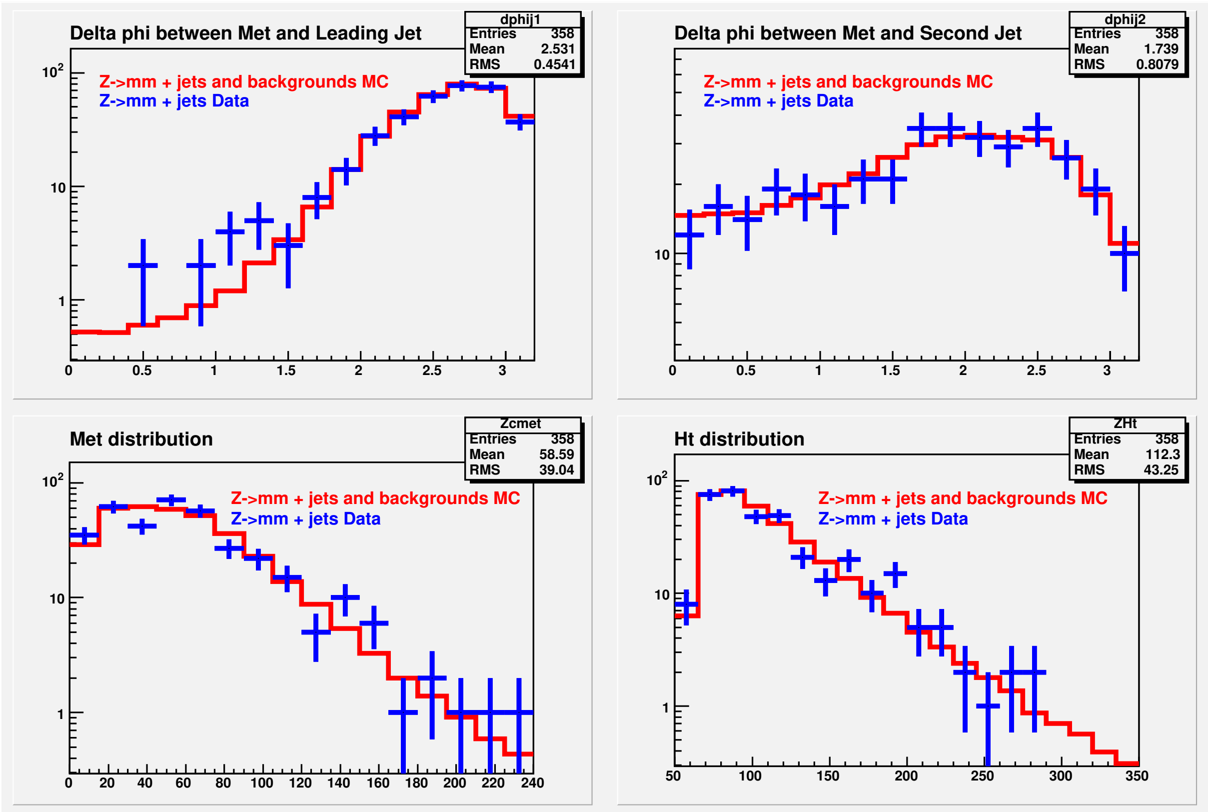

Figure 11: Comparison of jet kinematic distributions (II) between Alpgen Monte Carlo and data for $Z \to \mu\mu$+jets candidate sample.

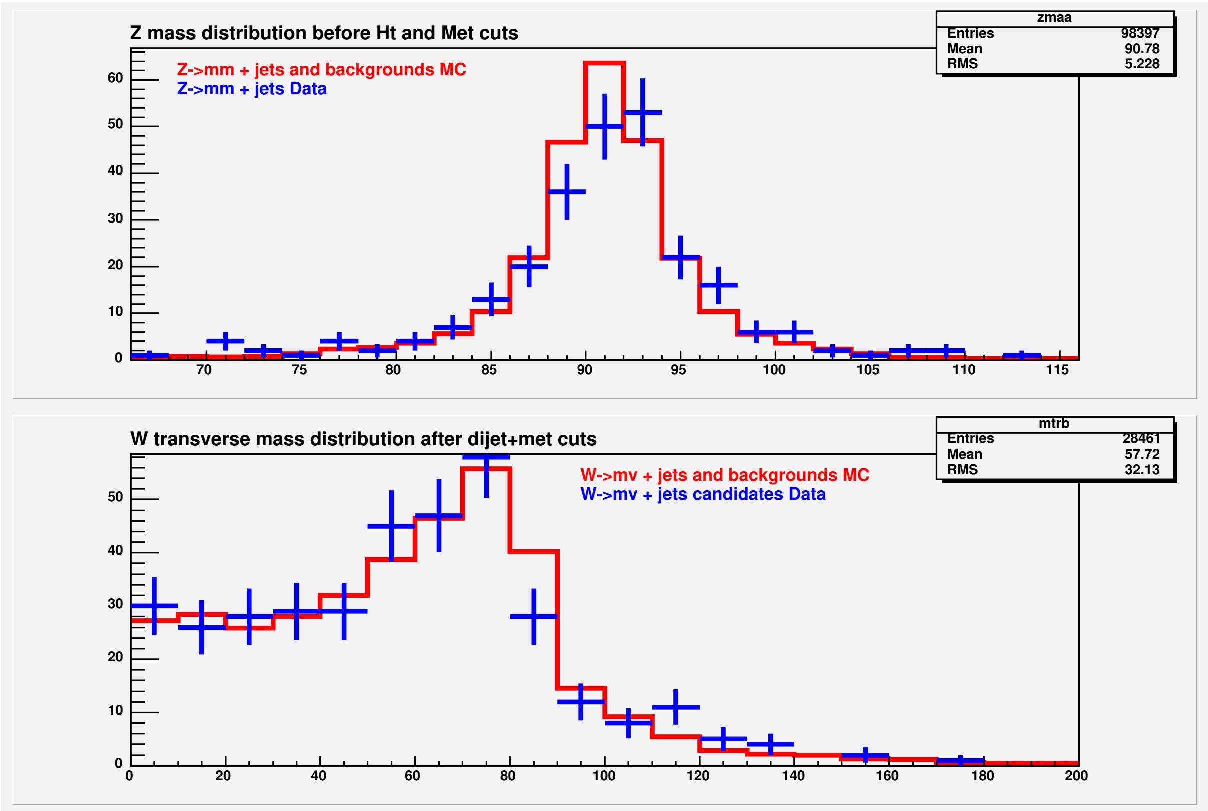

Figure 12: Comparisons of the Z invariant mass (top) and W transverse mass (bottom) distributions between Alpgen Monte Carlo and data for $Z \to \mu\mu$+jets and $W \to \mu\nu$+jets candidate samples.

3.2 QCD Background

QCD multijet events can pass our selections if one or more jets are badly mismeasured. Because of our $\Delta\phi$ selections, at least one jet must be lost which means that it must have lost enough energy to fall below our jet counting threshold. We classify QCD background events into two main categories:

1. category 1: events where one jet is dominantly responsible for the observed $\not{E}_T$. In those events, the missing Et points in the general direction of the jet which is lost.

2. category 2: events where at least 2 jets contribute signficantly to the *met*. In those events, the $\not{E}_T$ does not point in the general direction of any jet. Note that since we ask for two jets, at least one jet also needs to be lost in this category.

According to the simulation, category 1 dominates for the selection cuts we have used. For this reason, the general strategy is to use the data to estimate the absolute contribution of the dominant category 1 events. Category 2 events are estimated using the simulation.

To measure the contribution of three-jet events where the third jet is lost completely, events are selected where the $\not{E}_T$ is close to the 3rd jet. We require $\Delta\phi(\not{E}_T - \text{jetphi3}) < 0.3$ radians. By studying the E_T distribution of the third jet as more and more of the jet E_T is lost, we can estimate how many events will have jets below our jet counting threshold. We will fit the 3rd jet E_T distribution and extrapolate in the region below the jet counting threshold. This region is populated with QCD background events from category 1.

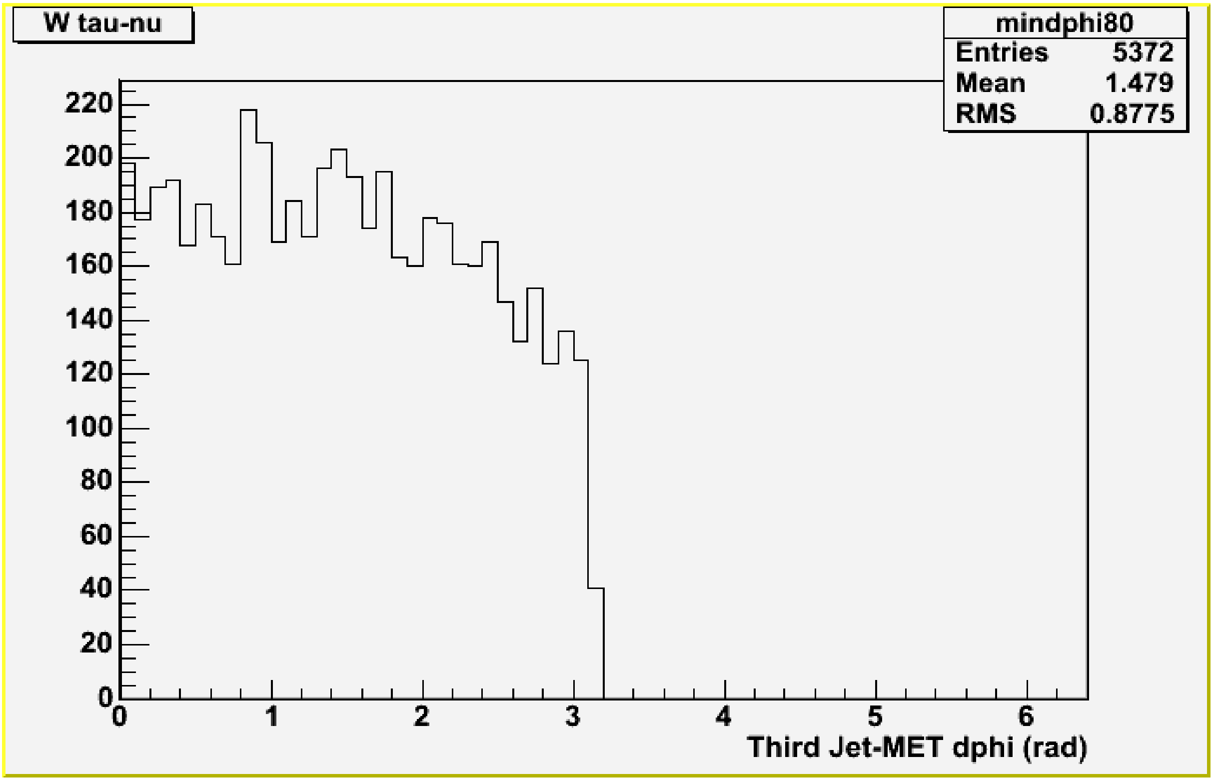

Figure 13: $\Delta\phi$ between met and the third jet in the event for $W \to \tau\nu$ events.

Before we perform the extrapolation in the data, we must apply corrections since, according to the simulation, the data normalization will receive signficant contributions from electroweak backgrounds. We use the data to normalize the level of electroweak contamination by studying the $\Delta\phi(\not\!\!E_T - \text{jetphi3})$ region between 0.0 and 0.5 radians. We note that about 98% of the QCD events in this region are between 0.0 and 0.3 radians. The electroweak background on the other hand is consistent with being flat in the region between 0.0 and 0.5 radians (see Figure 13 for $W \to \tau\nu$ and Figure 14 for $W \to \mu\nu$). We can therefore use the region between 0.3 and 0.5 radians as the electroweak normalization region. Since the distributions are flat, we will multiply the events observed in the region between 0.3 and 0.5 radians by 1.5 to estimate the number of electroweak events in the region between

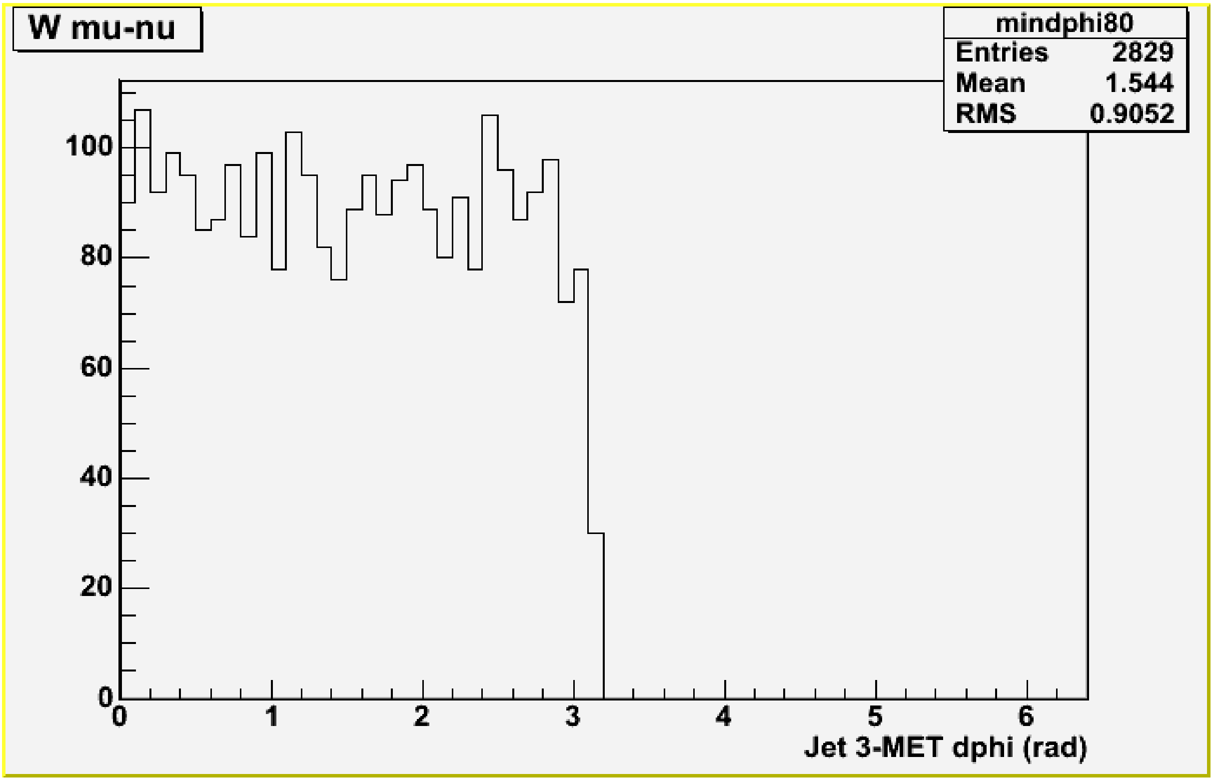

Figure 14: $\Delta\phi$ between *met* and the third jet in the event for $W \rightarrow \mu\nu$ events.

0.0 and 0.3 radians. Once we have this normalization, we need the shapes of the 3rd jet E_T distributions for those electroweak backgrounds. According to the simulation, the 3rd jet E_T distributions for our electroweak backgrounds are the same in the regions (0.0,0.3) and (0.3,0.5): mean and RMS values are the same. This allows us to use the distributions from the data itself in the region between 0.3 and 0.5. Using the data normalization and the data shapes obtained in this region, we are able to subtract the electroweak background in the region of interest (from 0.0 to 0.3 radians). A final correction needs to be applied to take into account the gamma + jet background. This background behaves very much like QCD with respect to its distribution in the $\Delta\phi$ region between 0.0 and 0.5 radians. For this reason, we use the sim-

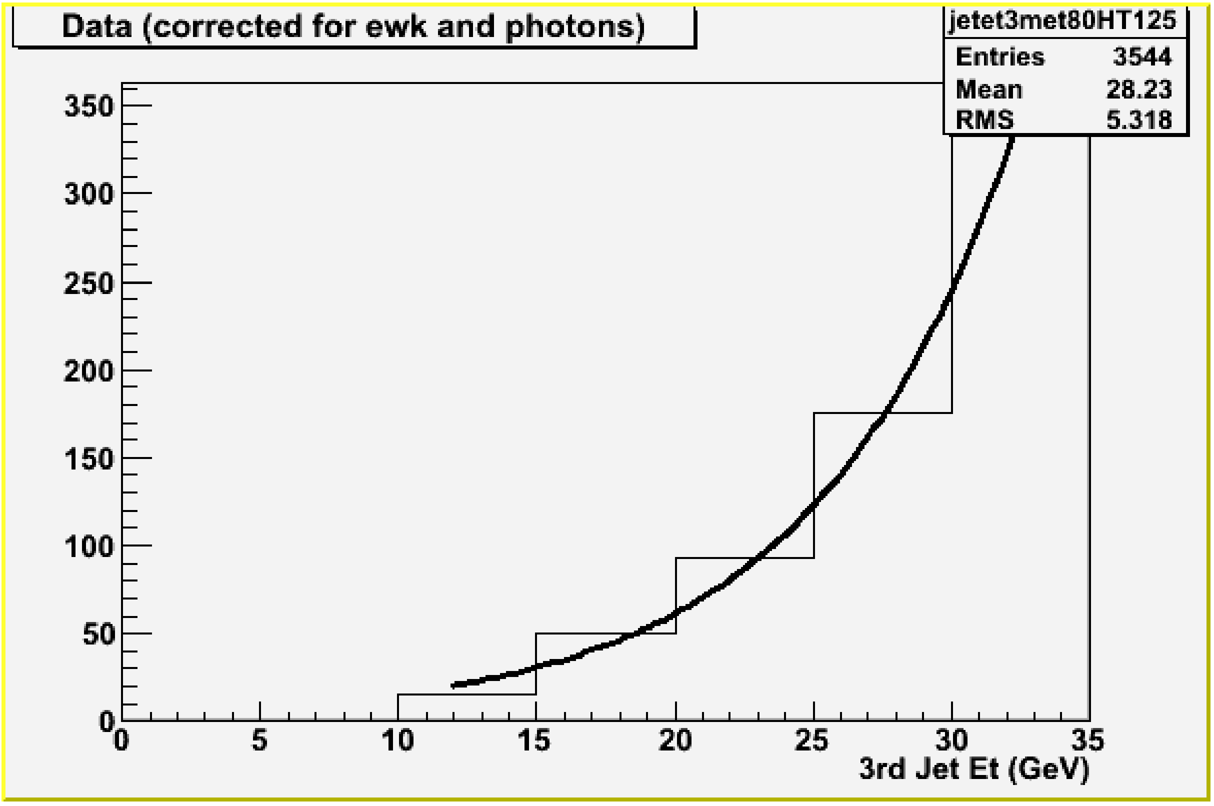

Figure 15: Fit to the 3rd jet E_T distribution in the data.

ulation to estimate the normalization and the shape in the region between 0.0 and 0.3.

The fitted distribution for the corrected data is shown in Figure 15. The number of events calculated to be below our threshold is 38.5. The simulation predicts that this category 1 contribution represents 78% of the total background. Category 2 events therefore represent 22% and are added to obtain a final estimate of the QCD background of 49 events. The systematic uncertainties add up to 30 events and include:

- a 50% uncertainty on the relative contribution of category 2 events i.e. $22 \pm 11\%$

- a relative variation of 10% (absolute value of 0.15) on the scale fac-

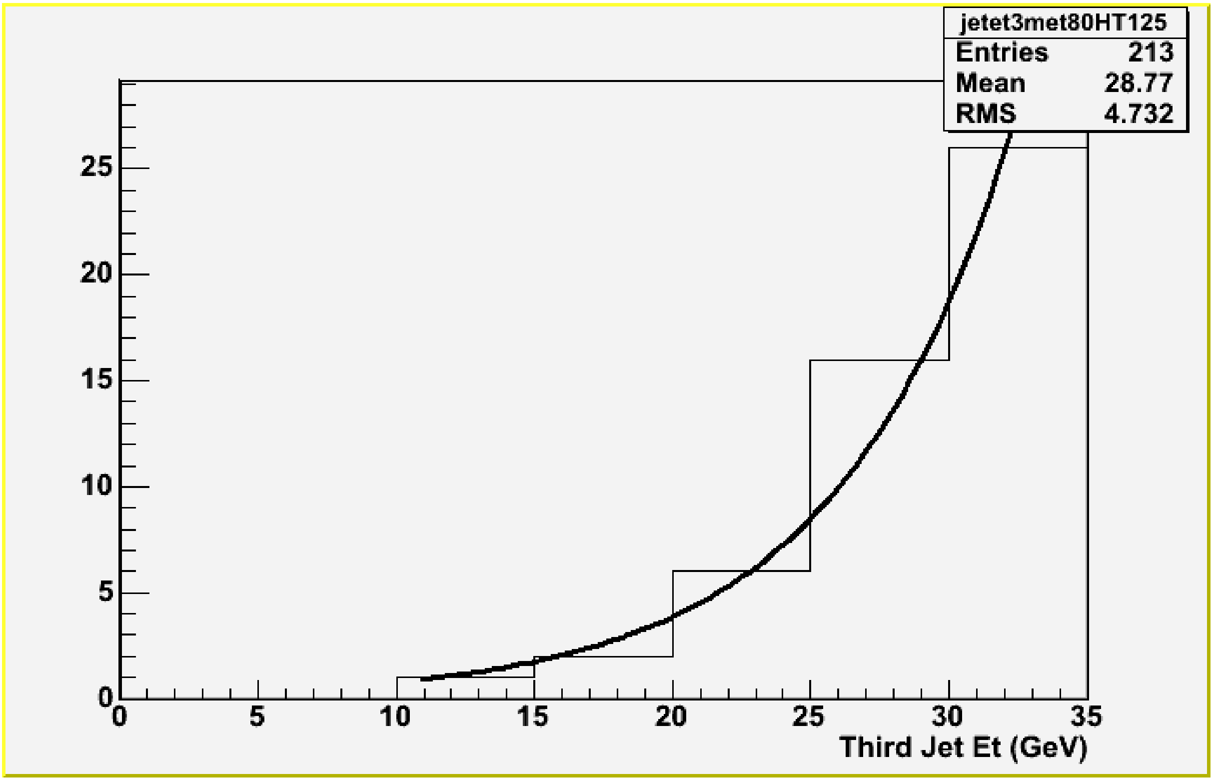

Figure 16: Fit to the 3rd jet E_T distribution in the simulation.

tor used to normalize the electroweak contribution. This value was set by comparing data-subtracted distributions to the general shape seen in the simulation. Around this value, the data distributions become inconsistent with a smoothly falling exponential distribution. The simulation distribution is given in Figure 16.

- We take half of the value of the correction obtained from gamma+jet events.

The calculation for the $H_T = 225$ and $\not{E}_T = 100$ region is done in the same manner after having verified that all the assumptions needed for the electroweak corrections were still valid. Our estimate is 9 events with an uncertainty of 9 events. The relative uncertainty is larger for this kinematic

$\not\!\!E_T$	predicted	obsreved
50	41	44
60	12	13
80	2	2

Table 8: Internal consistency check of the QCD background calculation.

region because of lower statistics in both our simulation and data samples.

We checked the internal consistency of the method in the simulation by predicting the number of QCD events that should pass all our selection cuts and then comparing this prediction to what we obtain after selections. The results for various $\not\!\!E_T$ cuts are given in Table 8

We also performed a simulation-driven estimate of the QCD background. The cross section used was that of PYTHIA multiplied by a K factor of 1.4 and only one event from the sample used survived. Scaled to the integrated luminosity of the data, this would corresponds to 60 ± 60 events which is consistent with our data-driven estimate.

3.3 Photon + jets Background

Events for which two high E_T jets are detected but a recoiling photon is lost in a crack of the detector constitute an additional background to our dijet+$\not\!\!E_T$ sample. The differential cross section for this process has been measured in Run I [30]. The production cross section for a photon with an E_T of at least 65 GeV was measured to be approximately 120$\pm$20 pb. This measured value, however, corresponds to a center of mass energy of $\sqrt{s}$ =1.8 TeV. In order to scale this cross section to its value at $\sqrt{s}$ =1.96 TeV, we increase it by (20$\pm$2)%. This factor has been estimated with the leading order calculation implemented in Pythia. We then compute the acceptance of γ+jets events to the selection criteria for our "dijet+$\not\!\!E_T$" candidate sample using Monte Carlo generated with a minimum p_T of 45 GeV, requiring that events entering the denominator of our acceptance calculation involve a photon of at least 65 GeV at the generator level. The γ+jets background contribution to our candidate samples can then be estimated by dividing the rescaled cross section by the product of this acceptance and the luminosity of the data sample. The largest contribution to the overall uncertainties on these estimates comes directly from the uncertainty on the scaled photon production cross section (16.7%). In addition, uncertainties from the Monte Carlo based acceptance measurement are incorporated. The most significant of these is the uncertainty on the Monte Carlo statistics which leads to a 13% relative uncertainty for the low kinematic region ($\not\!\!E_T > 80$ GeV, $H_T > 125$ GeV). In comparison, the uncertainty on the jet energy scale is 3 times smaller (4.3 %). Finally, since the cross section used to normalized the final predictions come from a Run I measurement, the uncertainty on the luminosity of the sample used to perform the Run I measurement and the luminosity of our MET45 data sample are essantially uncorrelated. We therefore add the usual 6% uncertainty on Run II luminosity measurement, in quadrature with the other sources of error. In the case of the search in the low kinematic region ($\not\!\!E_T > 80$ GeV, $H_T > 125$ GeV), the acceptance obtained for the full set of monojet selection criteria is (0.0190±0.0028)% which corresponds to a γ+jets background estimate of 54.8±12.8 events. For the search in the higher kinematic region ($\not\!\!E_T > 100$ GeV, $H_T > 225$ GeV) we obtain a background estimate of 4.7±2.6 events.

4 The Analysis

Before turning to the final analysis, we summarize the results up to this point. The data selection requirements (discussed in Section 2) are designed to produce high purity samples with two energetic jets and missing energy. The missing E_T and H_T thresholds chosen for the low kinematic region are based on the MET45 trigger turn-on curve (events with reconstructed missing E_T greater than 80 GeV are nearly 100% efficient). For the high kinematic region, the H_T cut is chosen to be as high as possible while still allowing us to make a background estimate with an uncertainty of 10-15% using our data-driven method. The indirect lepton veto, discussed in Section 2 increases the sensitivity to potential new physics by reducing the W+jets background contribution. The rest of the analysis path is based on the kinematics and aims at increased sensitivity for potential new physics signals.

4.1 Summary of SM Backgrounds with Jets+$\not\!\!E_T$

The Standard Model processes with two energetic jets plus missing energy in the final state have been discussed in detail in Section 3. They are summarized again here briefly.

- Z+jets : QCD associated Z production with $Z \rightarrow \nu\nu$ is the most significant and irreducible background component. For the Z+jets backgrounds, W/Z+jets data with decays to electrons and muons have been used to estimate the background as described in Sections 3.1.2- 3.1.3.

- W+jets : QCD associated W production with contributions from the $W \rightarrow e\nu$, $W \rightarrow \mu\nu$, and $W \rightarrow \tau\nu$ decay channels. The same samples used for the $Z \rightarrow \nu\overline{\nu}$ background are utilized to determine the W+jets backgrounds as described in Section 3.1.4.

- $t\bar{t}$ and single top production : Top quark events in which the W bosons from top decay leptonically can mimic the signal topology via the same mechanisms as QCD W+jets events. Top backgrounds are estimated directly from Monte Carlo as discussed in Section 3.1.5.

- QCD : The different topologies contributing to the QCD background are studied in Monte Carlo, and the overall contribution is determined from the data by studying three jet events where the $\not\!\!E_T$ is closely aligned with the smallest E_T jet in the event. The procedure is discussed in Section 3.2.

- γ+jets : The background contribution associated with the production of a photon plus a jet is estimated using an extraploation based on a Run I measurement of the inclusive photon cross section in conjunction with a Monte Carlo estimate for the fraction of the high p_T photon events that satisfy our selection criteria.

4.2 Additional Backgrounds from Non-Collision Sources

We expect that a few events from non-collision sources such as cosmic rays and beam-related backgrounds will make it into our final candidate samples. A small fraction of these events, especially those that overlap with real collisions, have a non-negligible probability for surviving the cleanup cuts used in this analysis. We use timing information available from the hadronic calorimeter to estimate these small, residual backgrounds. We look for events with hadronic energy deposits (in this case single hadron calorimeter towers above 5 GeV) that are measured to arrive more than 40 ns out-of-time with respect to the nearest collision but less than 80 ns out-of-time with respect to the same collision. The upper limit on the out-of-time requirement is made to avoid energy deposits associated with neighboring collisions. We compare the fraction of events with out-of-time deposits in our final candidate samples with those in the corresponding W/Z plus jets event samples which are expected to contain negligible contributions from non-collision backgrounds. In the end, we observe roughly the same fraction of events of this type in the W/Z+jets samples and the final dijet plus missing E_T sample. In the low kinematic region candidate sample, we observe $0.29 \pm 0.11\,\%$ events of this type versus $0.28 \pm 0.28\,\%$ in the corresponding W/Z+jets samples, consistent with a non-collision background of 4 ± 4 events. In the high kinematic region we observe a single event with out-of-time deposits in the candidate sample and no events in the corresponding W/Z+jets samples and therefore estimate a non-collision background of 1 ± 1 event.

As discussed previously in Section 2, we also run a cosmic track fitting algorithm on each event to check for potential cosmic ray track candidates. All reconstructed tracks with $p_T > 10.0$ GeV/c within each event are passed as inputs to the algorithm, which attempts to construct an extended track passing through two opposite hemispheres of the detector along a common trajectory based on the seed track direction. In cases where such a track is found, the algorithm outputs a χ^2 corresponding to the overall quality of the fit for the extended track. In order for an event to be tagged as a cosmic candidate, we require a minimum of one such track with a $\chi^2 < 1000$ to be found within the event. Using this cut, we find a total of 3 potential cosmic candidates in the low kinematic region data candidate sample. Our cut value of 1000 is somewhat arbitrary. We know that in busy events with large numbers of reconstructed tracks, there is a non-negligible probability that the cosmic algorithm will identify two nearly back-to-back tracks as a single, common track passing through both ends of the detector. In order to understand if our cosmic candidates should be treated as additional background, we look at events in our $W \to e\nu + \text{jets}$ sample (which we believe is a pure sample of beam-produced events) to see how often these are being mis-tagged as cosmics using our default criteria. In this sample, we find that 2/508 events ($0.39 \pm 0.27\,\%$) are in fact being tagged as cosmics. This rate is actually higher than what we observe in the dijet plus missing E_T candidate sample where we tag 3/2506 events ($0.12 \pm 0.07\,\%$). Since this tagging rate is lower than what we observe in the pure sample of beam-produced events, we choose to not treat the cosmic candidates in our sample as background events. Also note that none of the events in the high kinematic region are tagged as cosmics.

We also find 5/2506 events in the low kinematic region candidate sample for which the best quality event vertex used in our event selection process is not the same as the vertex used in jet clustering. Since we are attempting to select events based on the presence of high E_T jets, our main concern is that the vertex used in the jet clustering is in fact the correct one so that the jet E_T values are not being calculated incorrectly. We scanned each of the 5 events by eye using the CDF event display program. For each event, we were able to determine that the event vertex used in the jet clustering was in fact the one from which the high E_T jets in the event most likely originated. Since we believe that the jet E_T values in these events are correct, we choose to treat these as good signal events and do not remove them from our candidate sample. The total non-collision background estimates used for each of the

Background	$H_T > 125, \not\!\!E_T > 80$	$H_T > 225, \not\!\!E_T > 100$
$Z \to \nu\overline{\nu}$	777 ± 49	71 ± 12
$W \to \tau\nu$	669 ± 42	50 ± 8
$W \to \mu\nu$	399 ± 25	33 ± 5
$W \to e\nu$	256 ± 16	14 ± 2
$Z \to \ell\ell$	29 ± 4	2 ± 0
Top Quark Production	74 ± 9	11 ± 2
QCD	49 ± 30	9 ± 9
γ+jet	55 ± 13	5 ± 3
Non-collision	4 ± 4	1 ± 1
Total predicted	2312 ± 140	196 ± 29
Data observed	2506	186

Table 9: Summary of estimated Standard Model background contributions to the dijet plus missing E_T candidate samples along with the number of observed events in data.

candidate samples are therefore simply those obtained from our studies of out-of-time events based on hadron calorimeter timing information.

4.3 Background Predictions

A summary of our background estimates for the various SM processes contributing to the dijet plus missing E_T candidate samples is shown in Table 9. In the low kinematic region we predict a total background of 2312 ± 140 and observe 2506 events in the data (1.3σ excess). Comparisons of the event missing E_T, jet H_T, leading jet E_T, trailing jet E_T, leading jet η, trailing jet η, and jet $d\phi$ distributions for the 2506 events in this candidate sample with the expected distributions from the SM backgrounds are shown in Figs. 17 - 23. The comparisons of the event missing E_T and jet H_T distributions are also shown in Figs. 24 and 25 on a log scale including the stacked contributions of each individual SM background process. In addition, we make direct shape comparisons of the event missing E_T and jet H_T distributions in data and Monte Carlo for the low kinematic region sample by normalizing the SM prediction to match the number of observed events in data. These comparisons are shown in Figs. 26 and 27. In the high kinematic region we predict a total background of 196 ± 29 events and observe 186 events in data; and therefore conclude that no excess is present in the data. Comparisons of the event missing E_T, jet H_T, leading jet E_T, trailing jet E_T, leading jet η, trailing jet η, and jet $d\phi$ distributions for the 186 events in this candidate sample with the expected distributions from the SM backgrounds are shown in Figs. 28 - 34. In the high kinematic region, we also examine the effect of removing each of the main kinematic selection criteria (event missing E_T and jet H_T). A comparison of the event missing E_T distribution after removal of the missing E_T cut between the SM prediction and data is shown in Fig. 35. Note that the Monte Carlo shape associated with each background process is normalized to its estimated contribution within the dijet plus missing E_T signal region. The large data excess in the missing E_T region below 100 GeV is due to the lack of a model for the QCD background shape below the signal region. A similar comparison of the jet H_T distribution after removal of the jet H_T cut is shown in Fig. 36.

4.4 Limit Calculations

Based on the observed agreement between data and our SM background estimates, we can proceed to constrain the potential contribution from new physics sources. From the number of observed events, the predicted number of SM background events, and the uncertainty on this background prediction, we can set an upper limit on the number of signal events contributing to our candidate samples. In general, we can rule out a model that results in a production cross section times event acceptance which results in an expected signal contribution (based on the total integrated luminosity of the candidate sample) above this maximum allowed limit. However, the limit is also effected by any uncertainty on the event acceptance associated with a particular model (obtained from MC). Since this is first and foremost a signature based search, we quote 95% C.L. upper limits on the number of potential non-SM signal events in each of the samples for a wide range of potential acceptance uncertainties. Table 10 shows the limits obtained from the low kinematic region sample and Table 11 shows the limits from the high kinematic region sample. The quoted a priori limits are those that one would obtain for the case where the number of observed events agrees exactly with the total background prediction.

ΔA_{sig} (%)	A priori Upper Limit	Observed Upper Limit
7.5 %	288	452
10.0 %	292	459
12.5 %	297	469
15.0 %	303	481
17.5 %	311	495
20.0 %	320	513
22.5 %	331	533
25.0 %	345	558
27.5 %	360	587
30.0 %	378	621
32.5 %	399	660

Table 10: A priori and observed 95% C.L. upper limits on the number of non-SM signal events contributing to our low kinematic region candidate sample as a function of signal acceptance uncertainty.

ΔA_{sig} (%)	A priori Upper Limit	Observed Upper Limit
7.5 %	62	55
10.0 %	63	55
12.5 %	64	56
15.0 %	65	58
17.5 %	67	59
20.0 %	69	61
22.5 %	71	63
25.0 %	74	65
27.5 %	78	68
30.0 %	82	71
32.5 %	86	75

Table 11: A priori and observed 95% C.L. upper limits on the number of non-SM signal events contributing to our high kinematic region candidate sample as a function of signal acceptance uncertainty.

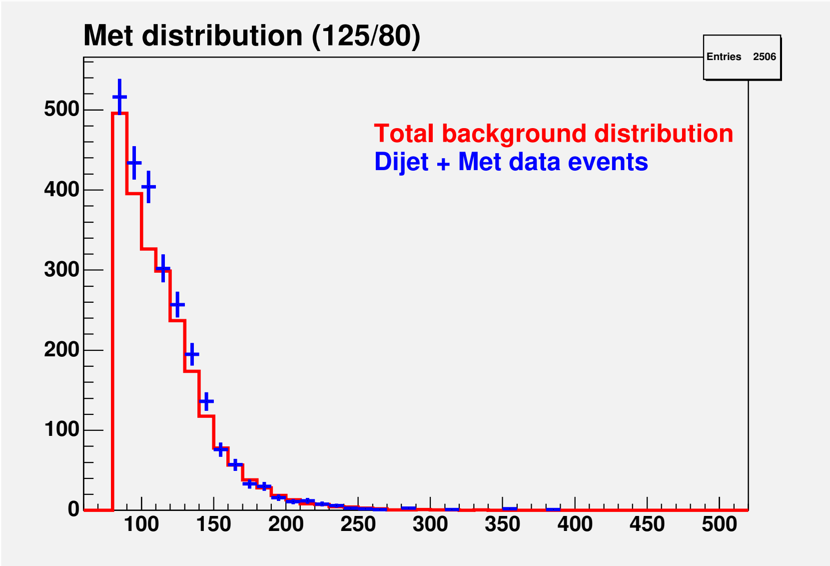

Figure 17: Comparison of the event missing E_T distribution for the 2506 events in the low kinematic region candidate sample with the predicted SM distribution.

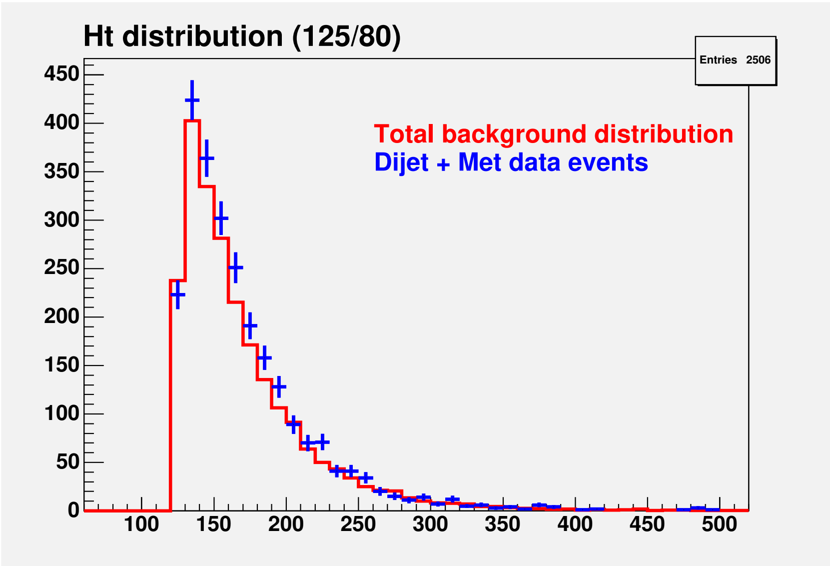

Figure 18: Comparison of the combined jet H_T distribution for the 2506 events in the low kinematic region candidate sample with the predicted SM distribution.

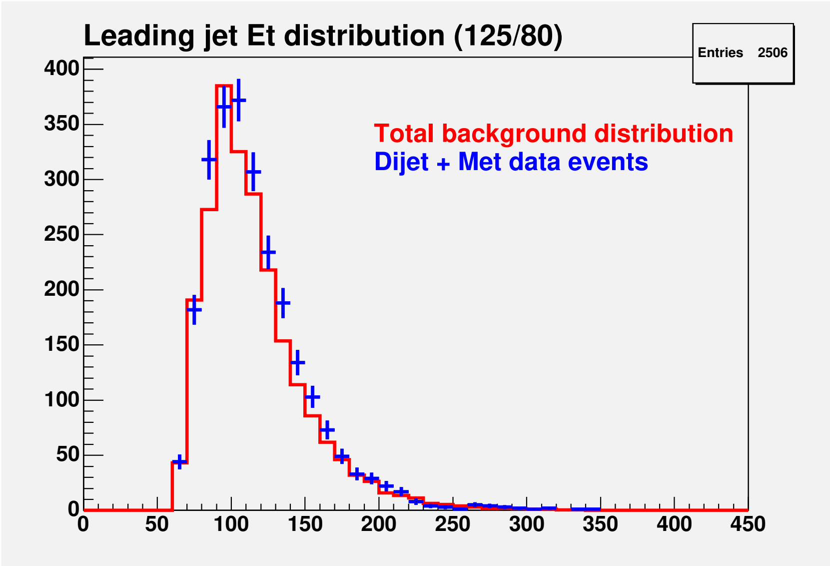

Figure 19: Comparison of the leading jet E_T distribution for the 2506 events in the low kinematic region candidate sample with the predicted SM distribution.

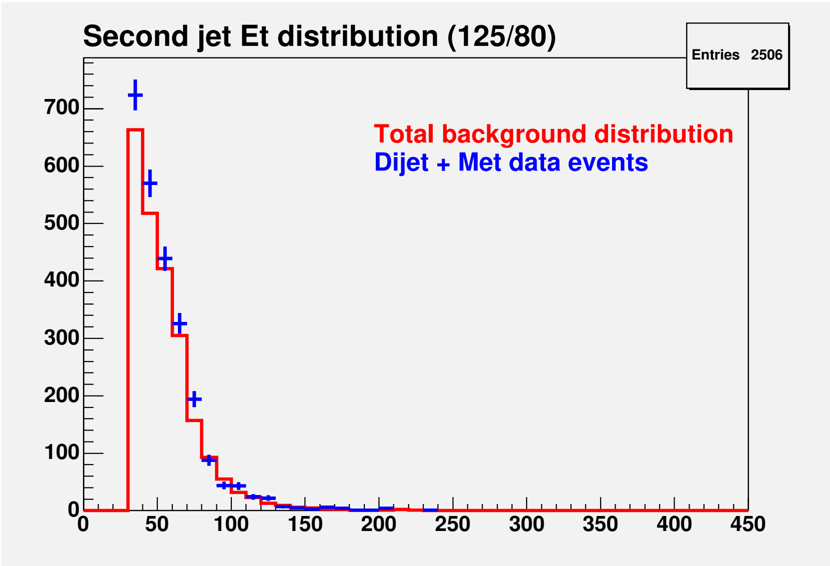

Figure 20: Comparison of the trailing jet E_T distribution for the 2506 events in the low kinematic region candidate sample with the predicted SM distribution.

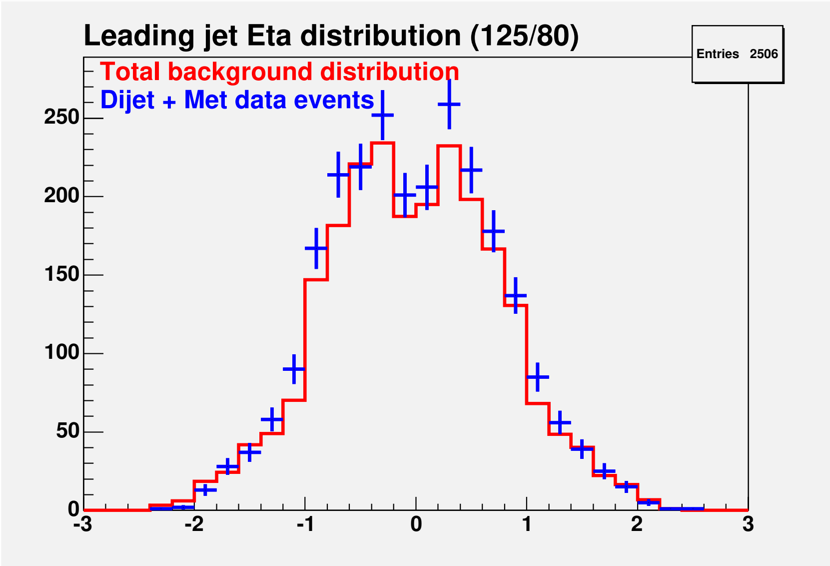

Figure 21: Comparison of the leading jet η distribution for the 2506 events in the low kinematic region candidate sample with the predicted SM distribution.

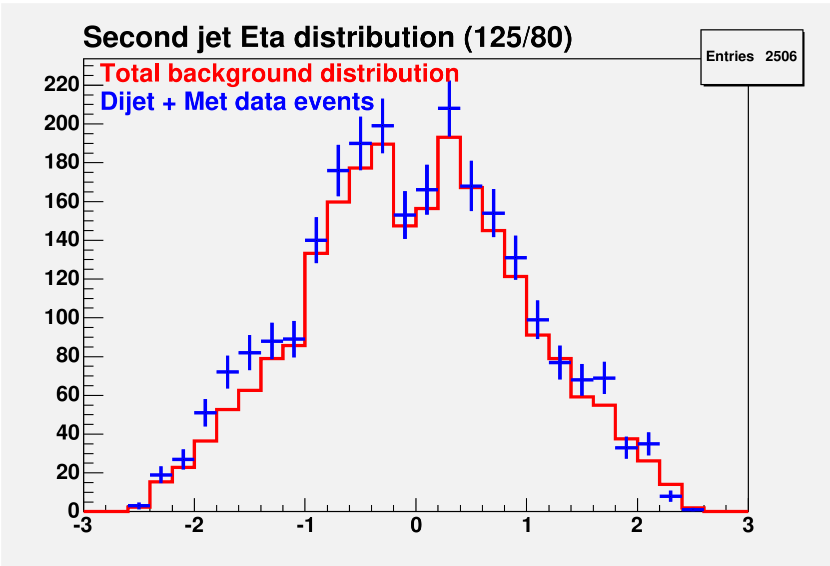

Figure 22: Comparison of the trailing jet η distribution for the 2506 events in the low kinematic region candidate sample with the predicted SM distribution.

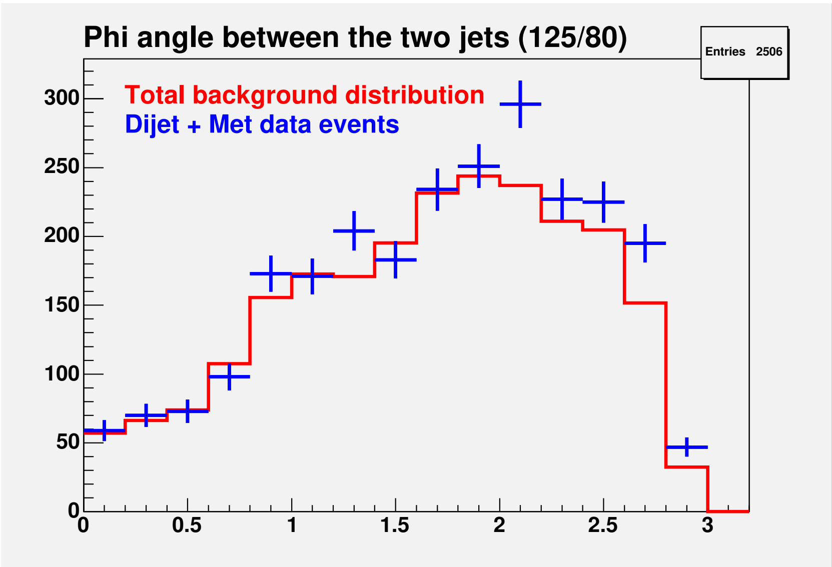

Figure 23: Comparison of the distribution for $d\phi$ between the two jets for the 2506 events in the low kinematic region candidate sample with the predicted SM distribution.

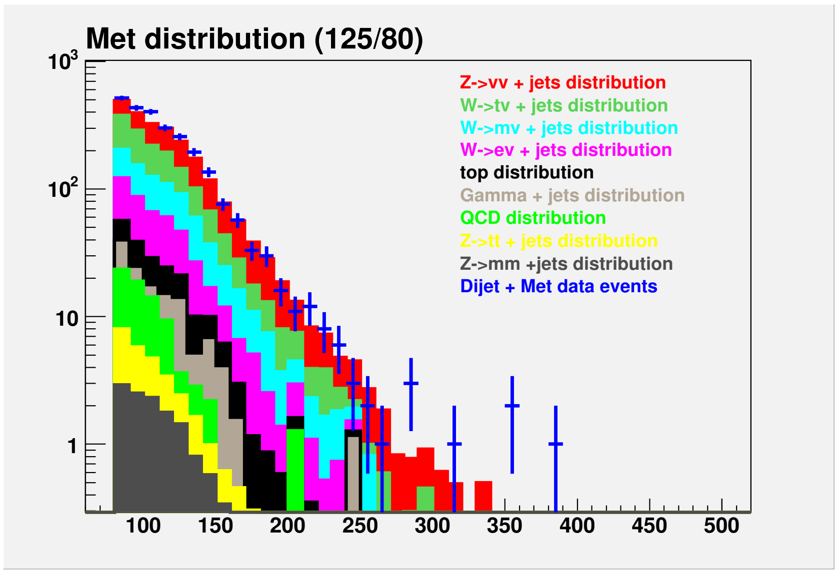

Figure 24: Comparison of the event missing E_T distribution for the 2506 events in the low kinematic region candidate sample with the predicted SM distribution showing the stacked contributions of each SM background process.

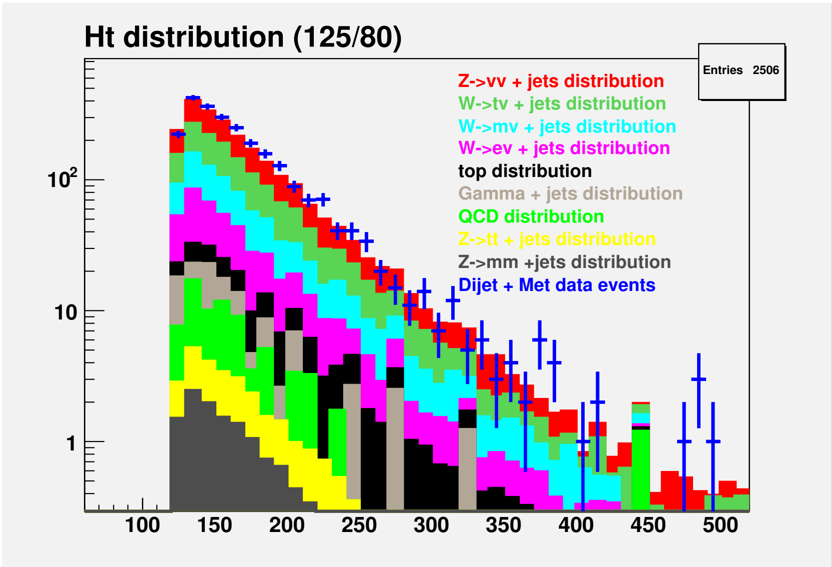

Figure 25: Comparison of the combined jet H_T distribution for the 2506 events in the low kinematic region candidate sample with the predicted SM distribution showing the stacked contributions of each SM background process.

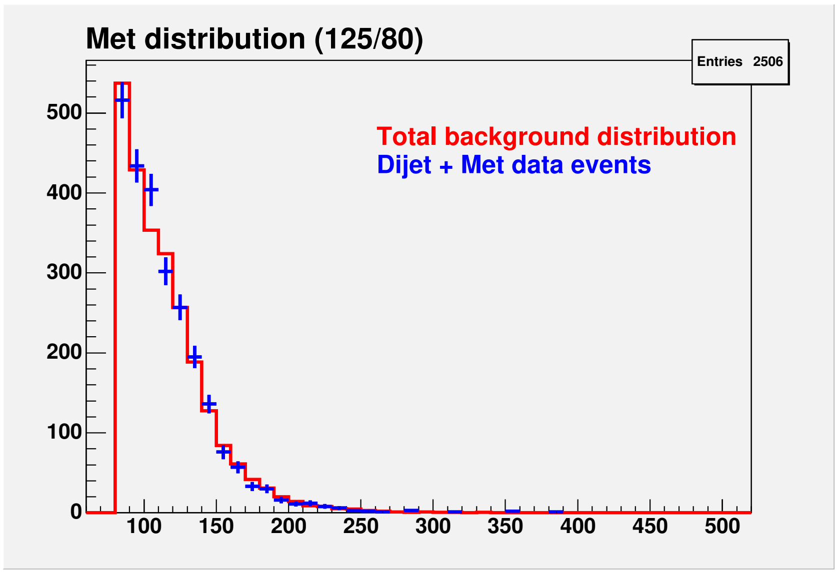

Figure 26: Shape comparison of the event missing E_T distribution between data and the SM prediction in the low kinematic region. The combined Monte Carlo shape is normalized to match the 2506 observed events in data.

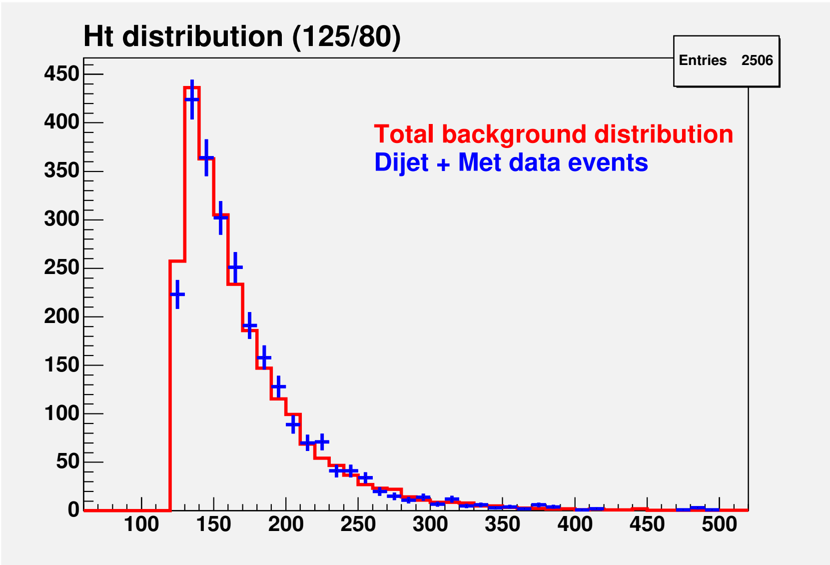

Figure 27: Shape comparison of the combined jet H_T distribution between data and the SM prediction in the low kinematic region. The combined Monte Carlo shape is normalized to match the 2506 observed events in data.

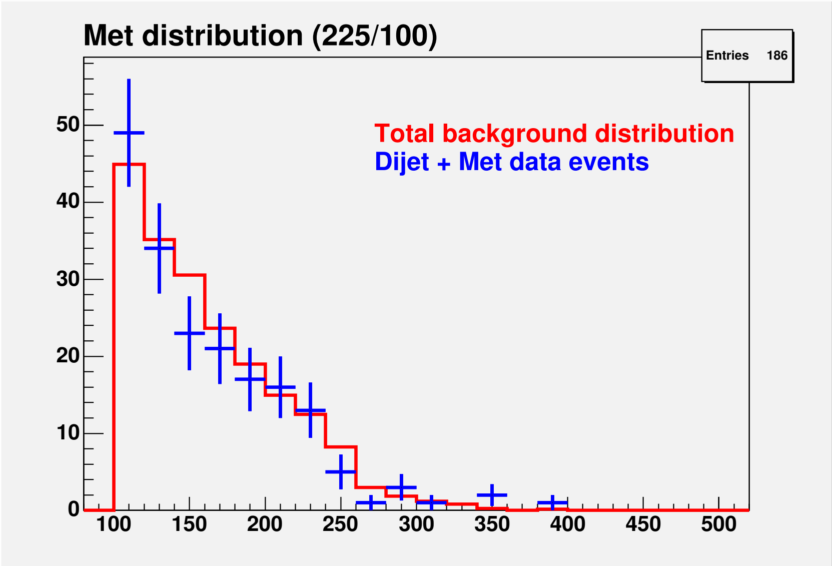

Figure 28: Comparison of the event missing E_T distribution for the 186 events in the low kinematic region candidate sample with the predicted SM distribution.

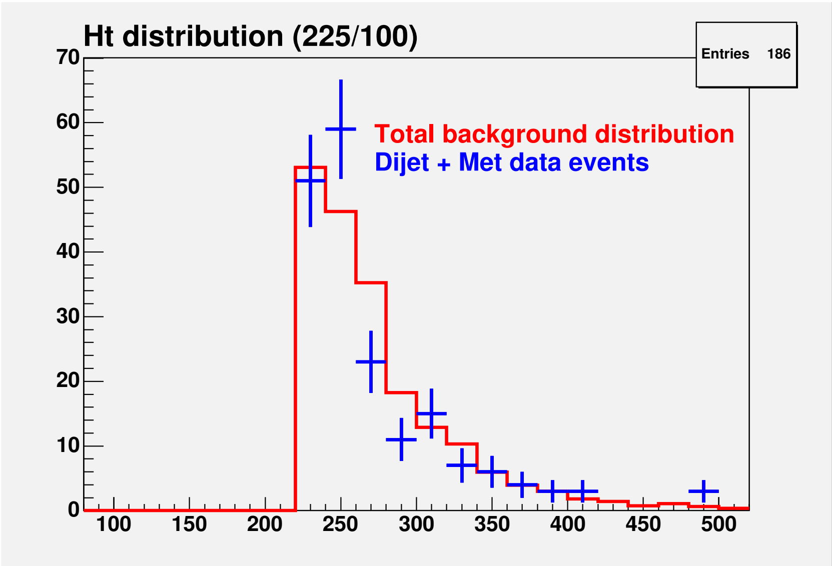

Figure 29: Comparison of the combined jet H_T distribution for the 186 events in the low kinematic region candidate sample with the predicted SM distribution.

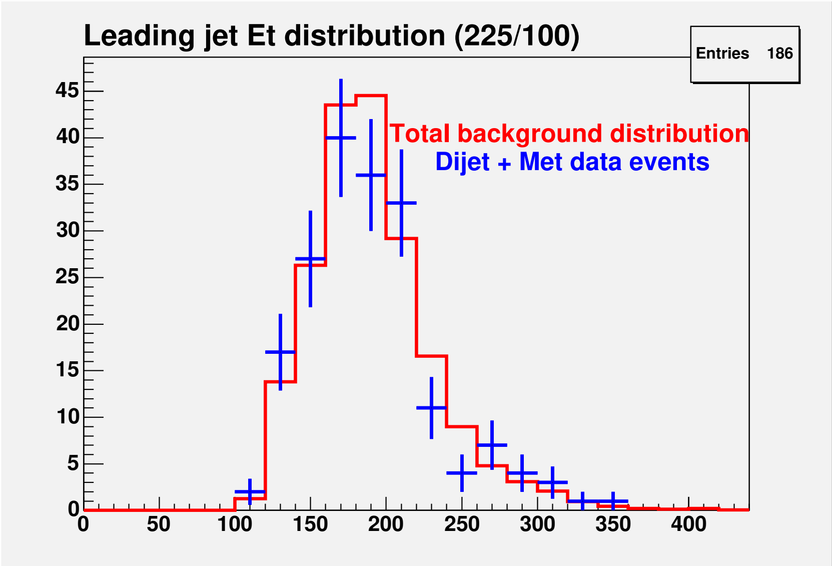

Figure 30: Comparison of the leading jet E_T distribution for the 186 events in the low kinematic region candidate sample with the predicted SM distribution.

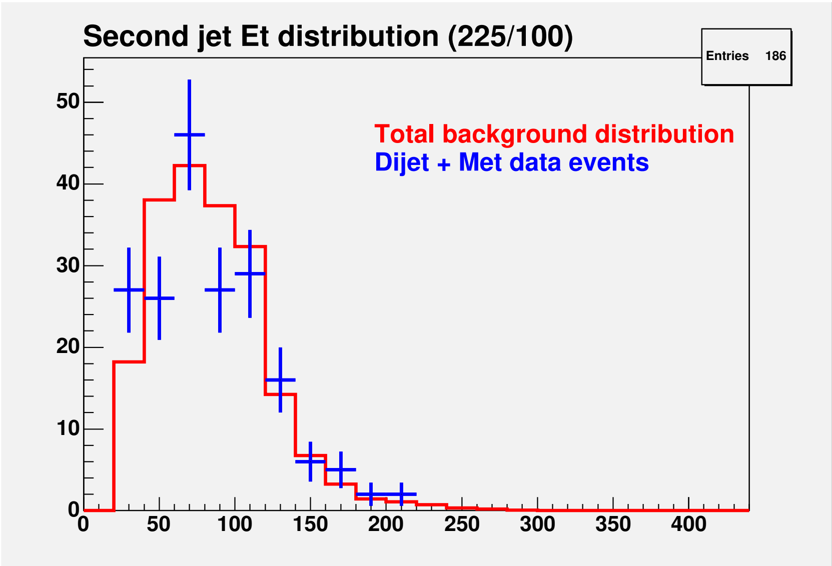

Figure 31: Comparison of the trailing jet E_T distribution for the 186 events in the low kinematic region candidate sample with the predicted SM distribution.

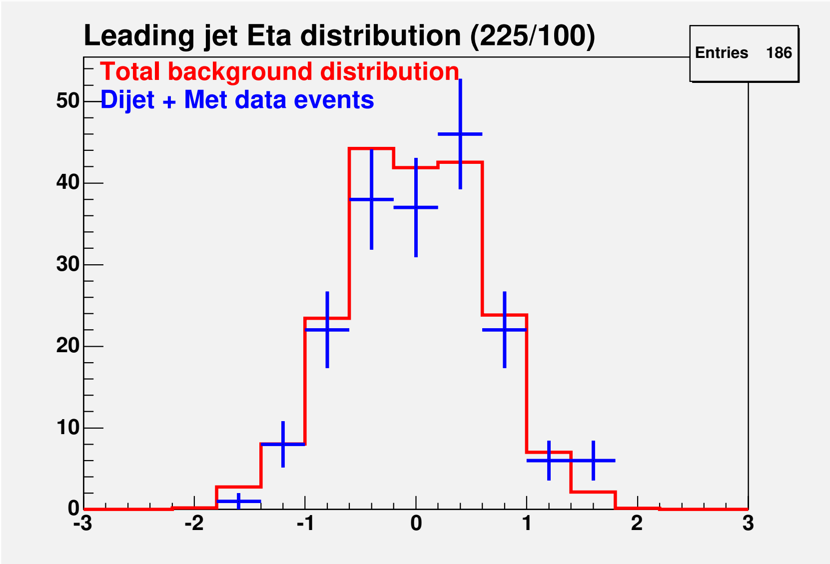

Figure 32: Comparison of the leading jet η distribution for the 186 events in the low kinematic region candidate sample with the predicted SM distribution.

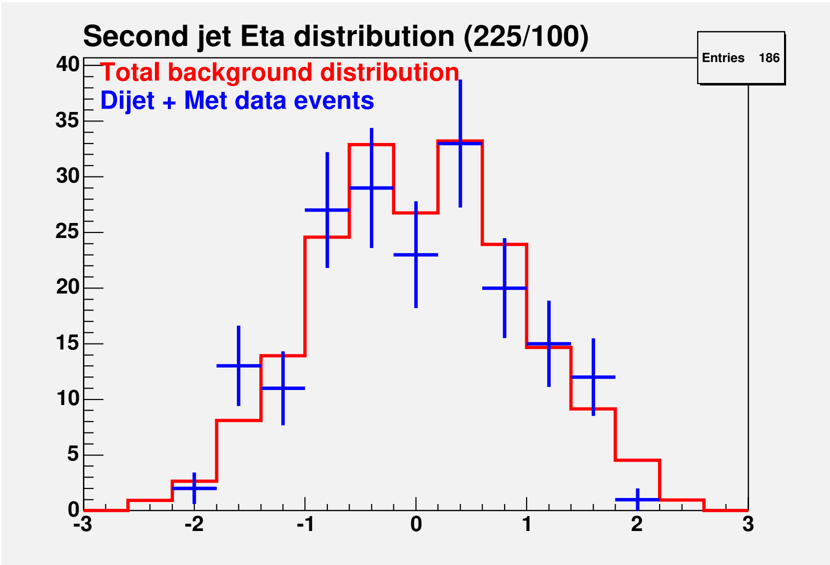

Figure 33: Comparison of the trailing jet η distribution for the 186 events in the low kinematic region candidate sample with the predicted SM distribution.

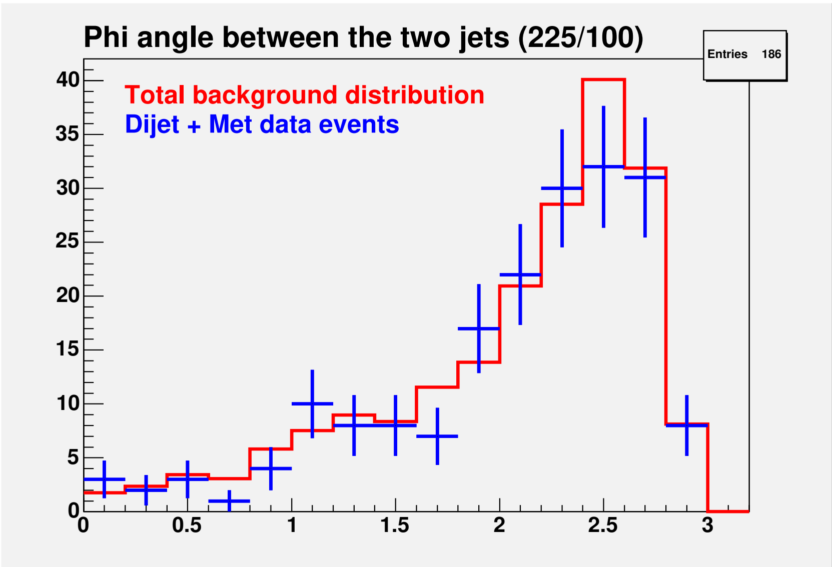

Figure 34: Comparison of the distribution for $d\phi$ between the two jets for the 186 events in the low kinematic region candidate sample with the predicted SM distribution.

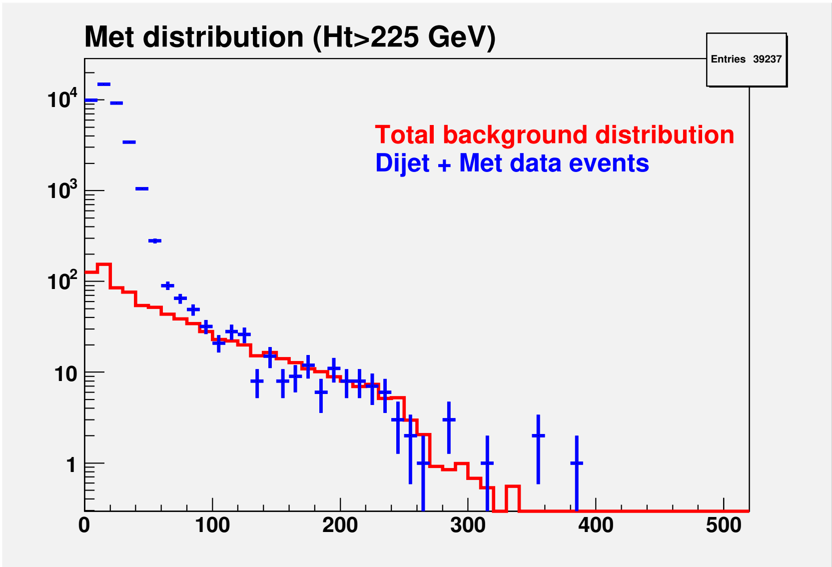

Figure 35: Comparison of the event missing E_T distribution between the SM predition and data in the high kinematic region after removal of the missing E_T selection cut. The Monte Carlo shape associated with each background process is normalized to its estimated contribution within the dijet plus missing E_T signal region. The large data excess in the missing E_T region below 100 GeV is due to the lack of a model for the QCD background shape below the signal region.

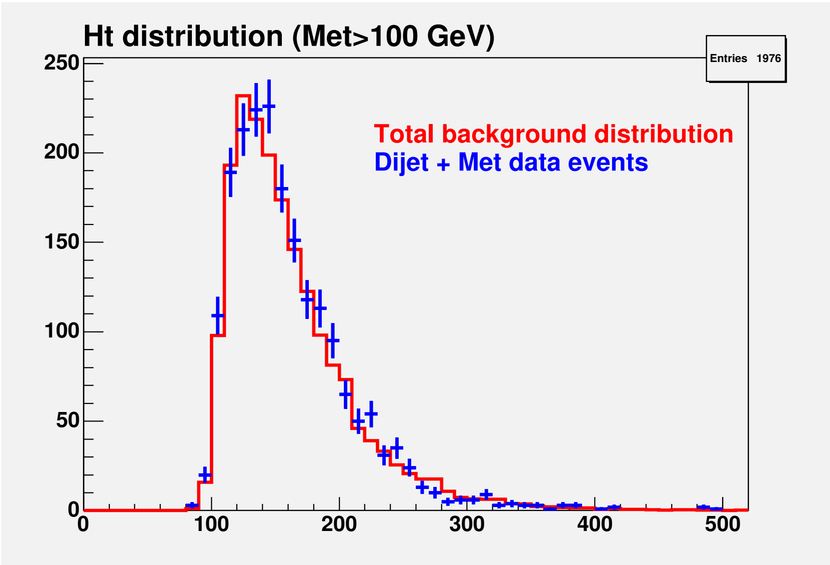

Figure 36: Comparison of the combined jet H_T distribution between the SM predition and data in the high kinematic region after removal of the jet H_T selection cut. The Monte Carlo shape associated with each background process is normalized to its estimated contribution within the dijet plus missing E_T signal region.

5 Leptoquark interpretation

In the previous section, we presented a priori and observed upper limits based on this analysis on the number of allowed signal events originating from new physics models over a wide range of signal acceptance uncertainties. Assuming that all the new physics events tolerable within our observation at 95% C.L. come from a unique source, we can use the above limits to constrain the parameters associated with any such model. Due to the model-independent nature of this analysis, limits can be set on a wide range of models that could contribute events to the dijet plus missing E_T signature. Here, we use the scalar leptoquark model to illustrate the potenital constraining power of our dijet plus missing E_T result on new physics models. In this section, we describe the details of the leptoquark model under consideration and in the following section provide details on the procedure used to extract the actual limits.

Leptoquarks are strongly interacting particles which carry both baryon and lepton numbers, allowing them to directly couple to both quarks and leptons. Leptoquarks therefore provide a link between the two known types of matter fields. Moreover, in the cases where the effective couplings to quarks and leptons are dimensionless, leptoquarks can in principal play a significant role in the renormalization of high energy theories since they provide a way to allow for cancellation of the triangle anomaly. Many different theories predict the existence of leptoquarks which manifest themselves at relatively small energies including Grand Unification theories as well as technicolor and string inspired models. In the following, we only consider effective leptoquark interactions, relying on the generic dependence of the low energy physics predictions as opposed to a detailed knowledge of the high energy theories themselves in order that the dependence of these predictions on a set of free parameters can be determined empirically. The constraints on parameters given in the following section will be based on this framework.

Although playing the game of effective theories allows for physics predictions without dependence on the particular theory from which the leptoquarks originate, some restrictions on possible leptoquark interaction terms and/or quantum numbers must be taken into account. There are three specific restrictions that apply to our phenomenological leptoquark model:

1. only dimensionless couplings with the matter fields are considered;

2. interaction terms are required to be gauge invariant;

3. allow only same generation couplings between lepton and quark.

The last requirement is based on the fact that experimental constrains on Flavor Changing Neutral Current (FCNC) decays and on the violation of the leptonic quantum number provided by measurements such as the anomalous magnetic moment of the muon and the ratio of $\frac{\sigma(\pi\to e\nu)}{\sigma(\pi\to\mu\nu)}$ are severe.

We also consider three additional restrictions which are not strcitly motivated by phenomenological constraints but serve to simplify the model under investigation while at the same time maintaining a high degree of generality:

1. consider only scalar leptoquark production;

2. assume that leptoquarks decay prior to fragmentation;

3. consider only leptoquarks that decay to a $q\nu$ final state with a branching fraction of one.

Here, we restrict our interpretation of the dijet plus missing E_T results to scalar leptoquarks to avoid the model-dependent introduction of anomalous couplings needed to describe vector leptoquarks. At hadron colliders (Tevatron, LHC) leptoquarks are produced in pairs, originating from either $q\bar{q}$ or gg collisions. The production rate, therefore, depends only on the strong coupling α_s and the mass of the leptoquarks (M_{LQ}). At the Tevatron, $\sim 90\%$ of all leptoquark pairs are produced via $q\bar{q}$ collisions (one single s-channel Feynman diagram). In considering leptoquarks (defined by a unique set of quantum numbers) that decay to a single final state, we remove any potential model dependence coming from the effective Yukawa coupling. In other words, if we were to parameterize the dependence on the Yukawa coupling in terms of the branching ratio β of an unstable leptoquark and multiply the scalar leptoquark production rate by $(1-\beta)$, the above restriction is equivalent to the assumption of $\beta = 0$. This model is therefore restricted to scalar leptoquarks carrying an electric charge of $\frac{1}{3}$ ($LQ \rightarrow \bar{d}\nu$) or $\frac{2}{3}$ ($LQ \rightarrow u\nu$). Conversely, cases where $\beta \neq 0$ correspond to leptoquarks of charge $\frac{-1}{3}$ and $\frac{-2}{3}$ where at the opposite extreme ($\beta = 1$) the resulting leptoquarks can only be studied in $jj\ell\ell$ final states.

By choosing to interpret our dijet plus missing E_T results in terms of a scalar leptoquark model with $\beta = 0$, we make the simplest possible choice (only one free parameter: M_{LQ}) and the most model-independent leptoquark interpretation possible. This model is therefore an ideal benchmark in the context of our signature-based, model-independent dijet plus missing E_T search. The main goal is to provide a simple example interpretation which is transparent and can be easily used by other phenomenologists to obtain reliable estimates of constraints on their favorite models.

The PYTHIA event generator (processes ISUB= 163 and 164) is used to simulate leptoquark samples for each generation based on our simple model. Leptoquark mass is set directly by assigning a value to the pmass(42,1) parameter in PYTHIA. The default generation is for a second generation leptoquark with electric charge of $\frac{1}{3}$ ($LQ \rightarrow \bar{s}\nu$). We generate samples for masses between 50 and 200 GeV/c^2 in steps of 10 GeV/c^2. Note that the current limits on scalar leptoquark production for the $jj\nu\nu$ final state are 117 GeV/c^2 for the first generation, 123 GeV/c^2 for the second generation, and 149 GeV/c^2 for third generation leptoquarks. Since the total production cross section only depends on α_s and M_{LQ}, the production rate applies to leptoquarks with charges of both $\frac{1}{3}$ and $\frac{2}{3}$ and for all generations. However, as discussed in the next section, there is a small generational dependence on signal acceptance originating from differences between light and heavy quarks in the final state. The production cross sections used in setting our limits are not the LO PYTHIA cross sections, but rather NLO cross sections calculated by Kramer *et al.* [31]. Table 12 shows the NLO cross sections obtained from Kramer for three different variations of the renormalization scale. For our analysis we choose to use the renormalization scale ($\mu = 2 \times M_{LQ}$) which gives the smallest production cross sections and hence the most conservative limits.

M_{LQ} (GeV)	$\mu = /frac12M_{LQ}$ (pb)	$\mu = M_{LQ}$ (pb)	$\mu = 2M_{LQ}$ (pb)
50 GeV	690.	584.	485.
60 GeV	270.	231.	192.
70 GeV	119.	103.	86.4
80 GeV	58.2	50.8	42.7
90 GeV	30.6	26.9	22.7
100 GeV	17.0	15.1	12.8
110 GeV	9.96	8.91	7.59
120 GeV	6.09	5.47	4.68
130 GeV	3.85	3.47	2.97
140 GeV	2.48	2.26	1.94
150 GeV	1.66	1.51	1.30
160 GeV	1.13	1.03	0.887
170 GeV	0.781	0.713	0.614
180 GeV	0.548	0.501	0.432
190 GeV	0.389	0.356	0.307
200 GeV	0.278	0.255	0.220

Table 12: Calculated NLO cross sections for different values of the leptoquark mass and three different potential values of the renormalization scale, μ.

6 Setting Limits on Leptoquarks mass

6.1 Calculation of the Limit

Based on the observed agreement between data and our SM background estimates, we can proceed to constrain the potential contribution from direct leptoquark production in the context of the effective model described in the previous section. From the number of observed events, the predicted number of SM background events, and the uncertainty on this background prediction, we can set an upper limit on the number of signal events contributing to our candidate samples. After obtaining the maximum number of signal events, we can rule out our leptoquark production model for leptoquark masses where the production cross section times event acceptance results in an expected signal contribution (based on the integrated luminosity of the candidate sample) above the maximum allowed limit. In the process of making this extrapolation, however, we also need to account for the systematic uncertainty on our estimate of the signal acceptance (obtained from MC). The final limit depends on the lowest allowed value of the signal acceptance (within its uncertainties) since this value leads to the smallest possible signal event contribution. The details of this procedure are given in the following sections.

6.2 Expected Leptoquark Signal After Final Selection

The final dijet plus missing E_T selection requirements are applied to the signal Monte Carlo samples to determine the expected number of signal events for each value of the leptoquark mass. Independent estimates are obtained for the low and high kinematic regions used in this analysis. The overall normalization of the Monte Carlo samples is based on Kramer's NLO cross sections calculated with $\mu = 2 \times M_{LQ}$ given in Table 12.

The specific procedure used to extract the expected number of signal events for each choice of leptoquark mass is to multiply the NLO production cross section by the selection cut acceptance determined from the corresponding Monte Carlo event sample and the total intergated luminosity of our data candidate sample. We also correct these event totals to account for the efficiency of the MET45 trigger path used in the selection of our dijet plus missing E_T candidate sample. The simulated missing E_T distribution for the leptoquark signal at each mass point is convoluted with the bin-by-bin measurement of the MET45 trigger efficiency shown in Fig. 1 to extract an overall trigger efficiency for each signal sample. The resulting combined trigger efficiency is above 99% for each of the samples. The final number of expected signal events for both the low and high kinematic regions as a function of the leptoquark mass is shown in Table 13.

6.3 Systematic Uncertainty on Signal Acceptance

As discussed previously, in order to set limits one also needs to determine the systematic uncertainty on the signal acceptance measurements obtained from the Monte Carlo samples. There are a number of different categories of uncertainties that we consider in determining the total uncertainty associated with the signal acceptance measurements for each of the kinematic regions used in our analysis. The techniques used to determine each component of the uncertainty are described below. Table 16 summarizes the final uncertainties associated with the signal acceptance measurements for each kinematic region.

M_{LQ}(GeV/c^2)	$H_T > 125$,$\not\!\!E_T > 80$	$H_T > 225$,$\not\!\!E_T > 100$
60	830	70
70	1020	108
80	1060	111
90	1026	134
100	980	124
110	868	124
120	749	124
130	604	114
140	473	104
150	364	93
160	281	84
170	213	73
180	156	60
190	120	52
200	89	42

Table 13: Expected number of signal events in both the low and high kinematic regions defined for the dijet plus missing E_T analysis as a function of leptoquark mass.

6.3.1 Choice of Structure Function

The default structure function we use is CTEQ5L [36]. We evaluate the uncertainty on the acceptance due to the choice of structure function following the prescription designed by Stephen Miller and approved by the Joint Physics group to evaluate such uncertainties [37]. The acceptance is compared with respect to the variations when using each of the forty CTEQ error pdfs [38]. In order to obtain a total PDF uncertainty, we sum variations in both the positive and negative directions from each of the error PDFs in quadrature. We then symmetrize the PDF uncertainty by taking the larger of the two quadrature sums for our final estimate. Currently, we are still in the process of obtaining the PDF uncertainty estimates for our generated samples. In the meantime, we take the values of the uncertainties quoted in the previous 200 pb^{-1} Run II analysis.

6.3.2 Jet Energy Scale

The calorimeter response has been carefully studied [41]. To evaluate this uncertainty, all jets in the signal Monte Carlo are rescaled by $\pm 1\sigma$, with the $\not\!\!E_T$ recalculated based on the rescaled jets. The upward and downward uncertainties due to the jet energy scale are determined by scaling all jets up or down and looking at the resulting changes in the acceptance. As in the case of the PDF uncertainty, we symmeterize the final jet energy scale uncertainty by taking the larger of the two changes.

6.3.3 ISR/FSR

The effects of gluon radiation are very important in this analysis. To evaluate the uncertainty on the acceptance from radiative effects, we use the solution devised by the top group from studies of Drell-Yan events [39]. We use the tcl files created by the top group [40], that are labeled as "more" or "less" and take a combined systematic for both ISR and FSR which is half the difference between the acceptances obtained using the "more" and "less" configuration for each.

To obtain the "more" and "less" configurations for the ISR systematic, the PYTHIA parameters PARP(61) (Λ_{QCD}) and PARP(64) (scale factor for the transverse momentum scale of ISR evolution) are varied based on studies of the p_T of the dilepton pair in Drell-Yan events. Similarly, for determining the "more" and "less" configurations for the FSR systematic, PARP(71) (scale factor for the Q^2 scale of the hard scattering) and PARP(72) (Λ value used in running α_s for parton showers) are varied.

6.3.4 Choice of Q^2 Scale

As mentioned previously, the NLO cross sections provided to us by Kramer are calculated for three different choices of the renormalization scale. Instead of taking an additional uncertainty on the choice of scale, we choose a more conservative approach which is to use the cross sections caluclated using the highest scale value, $\mu = 2 \times M_{LQ}$ for determining limits.

6.3.5 Luminosity

We assign the standard 6% uncertainty on the measured integrated luminosity of our data candidate sample.

6.3.6 Monte Carlo Statistics

We also assign a statistical uncertainty due to the finite size of the signal Monte Carlo samples used to determine the acceptances.

6.3.7 Efficiency of Clean-up Cuts

We allow for the possibility of a scale factor on the leptoquark signal acceptance to account for potential differences between the observed efficiencies of our event clean-up cuts in data and Monte Carlo. As summarized in Tables 14 and 15 for the low and high kinematic regions of the dijet plus missing E_T, respectively, we examine the effect of removing each individual clean-up cut on the total event yields for both data and Monte Carlo. Some fraction of the data events removed by each cut are presumably background, but we do not have a good method for determining this fraction for each of the applied cuts. Therefore, we assign a scale factor and associated uncertainty for each

Event Selection Cut	Data N-1	MC N-1	Scale Factor
Reconstructed Primary Vertex	N/A	+0.0 %	1.000 ± 0.000
6+ Tracks used to form Vertex	+0.2 %	+0.0 %	1.000 ± 0.002
$\lvert Z_{vtx}\rvert < 60$cm	N/A	N/A	0.996 ± 0.001
Event EM Fraction > 0.1	+1.0 %	+0.0 %	1.000 ± 0.010
Isolated Track Veto	N/A	+2.0 %	1.010 ± 0.010
Tracks matched to 2nd Jet ($\lvert\eta\rvert < 1.0$)	+2.8 %	+1.6 %	0.994 ± 0.006
Total			1.000 ± 0.017

Table 14: Determination of scale factors and associated uncertainties used to correct the signal acceptance obtained from Monte Carlo for measured event selection cut efficiencies in data for the low kinematic region defined in the dijet plus missing E_T analysis. A more detailed description of the procedure is provided in the text. Note that the scale factor uncertainties for the isolated track veto and 6+ tracks used to form vertex requirements are assumed to be correlated.

Event Selection Cut	Data N-1	MC N-1	Scale Factor
Reconstructed Primary Vertex	N/A	+0.0 %	1.000 ± 0.000
6+ Tracks used to form Vertex	+0.0 %	+0.0 %	1.000 ± 0.000
$\lvert Z_{vtx}\rvert < 60$cm	N/A	N/A	0.996 ± 0.001
Event EM Fraction > 0.1	+5.9 %	+0.0 %	1.000 ± 0.059
Isolated Track Veto	N/A	+3.6 %	1.018 ± 0.018
Tracks matched to 2nd Jet ($\lvert\eta\rvert < 1.0$)	+4.9 %	+2.1 %	0.986 ± 0.014
Total			1.000 ± 0.063

Table 15: Determination of scale factors and associated uncertainties used to correct the signal acceptance obtained from Monte Carlo for measured event selection cut efficiencies in data for the high kinematic region defined in the dijet plus missing E_T analysis. A more detailed description of the procedure is provided in the text. Note that the scale factor uncertainties for the isolated track veto and 6+ tracks used to form vertex requirements are assumed to be correlated.

Uncertainty Source	ΔA ($H_T > 125$,$\not\!\!E_T > 80$)	ΔA ($H_T > 225$,$\not\!\!E_T > 100$)
Jet Energy Scale	3.6%	6.0%
FSR	1.6%	2.6%
ISR	8.3%	6.5%
PDFs	4.0%	4.0%
Luminosity	6.0%	6.0%
MC Statistics	1.2%	2.4%
Clean-up Cuts	1.7%	6.3%
Total	11.9%	13.5%

Table 16: Relative systematic uncertainties on the signal acceptance obtained from the Monte Carlo for both kinematic regions defined for the dijet plus missing E_T candidate sample.

selection cut to cover the full range between the values obtained assuming that events removed in data originate either entirely from signal or background processes. For the reconstructed vertex requirement and our veto on events containing one or more isolated tracks, the large number of background events observable in data after the removal of these selection cuts force us to assume that the observed percentage of removed events in the Monte Carlo places an upper limit on the number of signal events removed in data. For these cases we believe this is a good assumption since data events are typically "noiser" and therefore contain extra tracks for forming vertices and additional energy deposition that typically results in tracks being less isolated. The scale factor for our selection cut on the z-position of the reconstructed vertex is taken from Willis Sakumoto's blessed numbers [45].

6.4 Determination of a priori limits

Because of the fact that we have performed separate searches in both the low and high kinematic regions defined for the dijet plus missing E_T candidate sample, we first need to determine which of the two regions will be used to set limits on our leptoquark model. The selection is made independently for each individual leptoquark mass point. Based on signal acceptance uncertainties of 11.9% for the low kinematic region and 13.5% for the high kinematic region, the a priori 95% C.L. upper limits on the number of potential non-SM events in our candidate samples are 295 and 64, respectively. Using these a priori upper limits, we determine that the low kinematic region is more sensitive for leptoquark masses of 130 GeV/c^2 and below, while the high kinematic region is more sensitive for mass points of 140 GeV/c^2 and larger. For the final limits, we always use the more sensitive of the two regions for determing whether a given mass point can or can not be excluded. After making this determination for each of the mass points, we then check to see which of the mass points will be excluded based on our a priori upper event limits. We find that all mass points between 60 and 170 GeV/c^2 will be a priori excluded.

6.5 Observed limits

The observed 95% C.L. upper limits on the number of potential non-SM events in our candidate samples based on signal acceptance uncertainties of 11.9% for the low kinematic region and 13.5% for the high kinematic region are 466 and 57, respectively. Based on these upper non-SM event limits, we are able to exclude all leptoquark mass points between 60 and 180 GeV/c^2. A linear extrapolation from 180 to 190 GeV/c^2 based on the expected number of signal events at each mass point allows us to determine a final lower limit on the leptoquark mass of 185 GeV/c^2. Note that this limit is for the 2nd generation, charge $\frac{1}{3}$ ($LQ \rightarrow \bar{s}\nu$) leptoquark used as the default for our signal

Monte Carlo generation. As mentioned previously, selection cut acceptance does vary slightly as a function of leptoquark generation. In order to quantify generational dependence, we also generated first and third generation signal samples for a few mass points. At 180 GeV/c^2 (the mass point closest to our limits), we find that the acceptance for a first generation leptoquark is 1.4% larger in the low kinematic region (6.0% larger in the high kinematic region). Conversely, for the third generation leptoquark the acceptance is 5.5% lower for the low kinematic region (17.5% lower for the high kinematic region). The observed differences in the acceptance values are primarily due to the lepton veto requirements used in the selection of the dijet plus missing E_T sample. Third generation production of b-quark jets is more likely to result in a secondary muon or electron which can result in the event being vetoed. We also looked at acceptance differences for the different generations at a lower mass value of 150 GeV/c^2 and found that the observed acceptance differences were smaller. Based on this trend, we can conservatively take the observed acceptance differences at 180 GeV/c^2 and apply them over the entire mass range in order to set independent limits on first and third generation leptoquark production. The procedure is to scale the expected number of events at each mass point using the measured acceptance difference and determine new limits based on the modified expectations. Based on this approach, we obtain a lower mass limit of 189 GeV/c^2 for first generation leptoquark production and 173 GeV/c^2 for third generation production. A summary of observed lower mass limits and corresponding upper limits on production cross sections is provided in Table 17.

LQ Model	Lower Mass Limit (GeV/c^2)	Upper Cross Section Limit (pb)
1st Generation	189	0.32
2nd Generation	185	0.37
3rd Generation	173	0.55

Table 17: 95% C.L. lower limits on scalar leptoquark mass for the different generations along with the corresponding upper limits on the leptoquark production cross sections.

7 Conclusion

We perform a search for new physics in the dijet plus missing E_T channel using 2 fb^{-1} of data. We obtain Standard Model background estimates of 2312 $\pm$ 140 events for our low kineamtic region candidate sample and 196 $\pm$ 29 events for our high kinematic region candidate sample. The number of observed data events in the two regions are 2506 (low) and 196 (high), consistent (at the $1.3\,\sigma$ level) with the original background estimates. In the case where we assume a 15% uncertainty on signal acceptance, we exclude at the 95% C.L. non-SM physics contributions greater than 481 events in the low kinematic region and 58 events in the high kinematic region. In the specific case of scalar leptoquark production, we extract 95% C.L. lower mass limits of 189 GeV/c^2 for 1st generation, 185 GeV/c^2 for 2nd generation, and 173 GeV/c^2 for 3rd generation production.

References

[1] P.-H. Beauchemin, K. Burkett, E. James, P. Savard, A. Yagil, *New Search for Extra Dimensions in Jets plus Missing Et above 80 GeV using 1.1 fb-1*, CDF Note 8715; A. Abulencia et al., The CDF Collaboration, *Search for Large Extra Dimensions in the Production of Jets and Missing Transverse Energy in $p\bar{p}$ Collisions at $\sqrt{s} = 1.96$ TeV*, Phys. Rev. Lett. 97, 171802 (2006), FERMILAB-PUB-06-079-E.

[2] For reviews, see for examples: L.M. Krauss, *The Standard Model, Dark Matter and Dark Energy: From the Sublime to the Ridiculous*, in the porceeding of the XIV Canary Islands Winter Shcool in Astrophysics, 2002 [astro-ph/0406673]; K.A. Olive, *TASI Lectures on Dark Matter*, in Summary of lectures given at the Theoretical Advanced Study Institute in Elementary Particle Physics at the University of Colorado at Boulder, 2002 [astro-ph/0301505].

[3] J.L. Feng, *Dark Matter at the Fermi Scale*, J.Phys. G32 (2006) R1 [astro-ph/0511043]

[4] R. Barbieri and A. Strumia, *The 'LEP paradox'* , from the IVth Rencontres du Vietnam (2000) [hep-ph/0007265]; S.F. King, *Beyond the Standard Model*, from the PLC2005 workshop (2005)

[5] H. Goldberg, Phys. Rev. Lett. **50**, 1419 (1983); J.R. Ellis, J.S. Hagelin, D.V. Nanopoulos, K.A. Olive and M. Srednicki, Nucl. Phys. B **238**, 453 (1984).

[6] G. Servant and T.M.P. Tait, Nucl. Phys. B **650**, 391 (2003) [hep-ph/0206071]; H.C. Cheng, J.L. Feng and K.T. Matchev, Phys. Rev. Lett. **89**, 211301 (2002) [hep-ph/0207125]

[7] H.C. Cheng and I. Low, JHEP **0309**, 051 (2003) [hep-ph/0308199]

[8] D. Acosta, J. Konigsberg, D. Tsybychev, S.M. Wang, *Search for Leptoquarks in the Jets and Missing Transverse Energy Topology*, CDF Note 7169; D. Acosta et al., The CDF Collaboration, *Search for First-Generation Scalar Leptoquarks in p anti-p Collisions at s**(1/2) = 1.96 TeV*, Phys. Rev. D72, 051107 (2005).

[9] F. Chlebana, G. Flanagan, A. Bhatti, J Dittmann, J. Huston, G. Latino, M. Martinez-Perez, R. Snihur, *First Measurement of the Inclusive Jet Cross Section in Run II*, CDF Note 6298.

[10] H. K. Gerberich, A. V. Kotwal and C. Hays. *Cosmic Ray Tagging using COT Hit Timing*, CDF Note 6089.

[11] D. Acosta *et al.* (CDF Collaboration), *Search for Kaluza-Klein Graviton Emission in $p\bar{p}$ Collisions at sqrts* $= 1.8$ *TeV using the Missing Energy Signature* Phys. Rev. Lett. **92**, 121802 (2004).

[12] An event is classified as a cosmic ray if the alogirthm finds a good “dicosmic fit” for either the incoming or outgoing cosmic hypothesis (diCosmicBestFit equals zero or one) with $\chi^2 < 1000$.

[13] E_{EM} = muon.emEnergy().

[14] E_{HAD} = muon.hadronEnergy().

[15] μ_{iso} = muon.coneR4Et().

[16] χ^2/n_{dof} = trk.chi2CT()/ (trk.numCTHits()- 5)

[17] $\eta_{\rm det}$ = emCluster $\rightarrow$ emEtaDetector()

[18] emobj-alg::conversion(emObject, 0, 0.2, 0.04) = 0

[19] e_{iso} = emCluster $\rightarrow$ totalIsolationEt4() - leakE where leakE is obtained from IsoCorrAlg::GetIsoCorr

[20] Δx = trkCESx - BestCESx where trkCESx = emobj-alg::TrackLocalCoord::vect(emObject, emTrack).x() and BestCESx = wire-cluster $\rightarrow$ localCoord() and wire-cluster is obtained from emObject.bestMatchingCesCluster()

[21] Δz = trkCESz - BestCESz where trkCESz = emobj-alg::TrackLocalCoord::vect(emObject, emTrack).z() and BestCESz = strip-cluster $\rightarrow$ globalCoord() and strip-cluster is obtained from emObject.bestMatchingCesCluster()

[22] Lshr = emobj-alg::CalculateLshr::lshr(*emCluster,strip-cluster $\rightarrow$ fitted-position(), emTrack $\rightarrow$ z0(), 3) where strip-cluster is obtained from emObject.bestMatchingCesCluster()

[23] χ^2_{strip} = scaleCesChisq(strip-cluster $\rightarrow$ chi2(), $E^{\rm clus}$) where strip-cluster is obtained from emObject.bestMatchingCesCluster()

[24] J.C. Long, H.W. Chan, and J.C. Price, preprint hep-ph/9805217.

[25] V.D. Barger and R.J.N. Phillips *Collider Physics, Frontiers in Physics*, Addison-Wesley(1997).

[26] D. Acosta et al., The CDF Collaboration, *First Measurements of Inclusive W and Z Cross Sections from Run II of the Tevatron Collider*, Phys. Rev. Lett. **94**,091803 (2005),

A. Abulencia et al., The CDF Collaboration, *Measurements of Inclusive W and Z Cross Sections in $p\overline{p}$ Collisions at $\sqrt{s} = 1.96$ TeV*, hep-ex/0508029, submitted to PRD.

[27] K. Burkett, E. James, P.-H. Beauchemin, P.-O. DeViveiros, and P. Savard, *An Estimate of the QCD Background to $W \to e\nu$ Events*, CDF Note 8722.

[28] Private communication with Steven Mrenna.

[29] Monte Carlo for FeMtobarn processes at Hadron Colliders. J. Campbell and K. Ellis. See `http://mcfm.fnal.gov/`.

[30] D. Partos, S. Kuhlmann and J. Lamoureux, *Run 1b Prompt Photon Cross Section*, CDF Note 4910.

[31] Private Communication with Kramer.

[32] K.Burkett, M. Spiropulu *Missing Energy Signature from Kaluza-Klein Graviton Emission With Run IB Data*, CDF Note 5151.

[33] Prakash Mathews, V. Ravindran, K. Sridhar, W.L. van Neerven *Next-to-Leading Order QCD Corrections to the Drell-Yan Cross Section in Models of TeV-Scale Gravity*, preprint hep-ph/0411018.

[34] Prakash Mathews, V. Ravindran, K. Sridhar, *NLO-QCD Corrections to Dilepton Production in the Randall-Sundrum Model*, preprint hep-ph/0506158.

[35] Private communication, Prakash Mathews and V. Ravindran.

[36] H.L. Lai et al, the CTEQ Collaboration, *Global QCD Analysis of Parton Structure of the Nucleon: CTEQ5 Parton Distributions*, Eur.Phys.J. **C12** (2000).

[37] Oscar Gonzalez and Carsten Rott, *Uncertainties due to the PDFs for the gluino-sbottom search*, CDF Note 7051.
`http://cdfrh0.grid.umich.edu/~miller/pdf/pdf_acceptance.html`

[38] `http://cdfrh0.grid.umich.edu/~miller/pdf/CTEQ6Pdf.txt`.

[39] Un-ki Yang, Y.K.Kim *Initial state gluon radiation studies on Drell-Yan data for top-pair production in hadron collider*, CDF Note 6804.

[40] See for example
`http://www-cdf.fnal.gov/~danielw/topmc5/tcl/mc_Pythia_ISRless.tcl.html`
`http://www-cdf.fnal.gov/~danielw/topmc5/tcl/mc_Pythia_FSRmore.tcl.html`

[41] Jet Energy and Resolution Group, *Generic Jet Scale Corrections for Run II*, CDF Note 7358.

[42] John Conway and Kaori Maeshima,*Poisson Upper Limits Incorporating Uncertainties in Acceptance and Background*, CDF Note 4476.

[43] Particle Data Group (K. Hagiwara *et al*), Phys. Rev. D 66 (2002) 010001.

[44] F. Abe et al., The CDF Collaboration, *Properties of Photon Plus Two-Jet Events in p anti-p Collisions at* $\sqrt{s} = 1.8\ TeV$ Phys. Rev. D, April 23, 1997, FERMILAB-PUB-97/106-E.

[45] W. Sakumoto, *Event* $|Z_{vtx}| < $ *60cm Cut Acceptance for Run II (to Feb06)*, CDF Note 8318

[46] E. G. Adelberger, B. R. Heckel, and A. E. Nelson, *Tests of the Gravitational Inverse-Square Law*, Ann.Rev.Nucl.Part.Sci. 53 (2003) 77-121.

[47] C. D. Hoyle, D. J. Kapner, B. R. Heckel, E. G. Adelberger, J. H. Gundlach, U. Schmidt, H. E. Swanson, *Sub-millimeter Tests of the Gravitational Inverse-square Law*, Phys. Rev. D**70** 042004 (2004).